Evaluation of two approaches for the synthesis of hierarchical micro-/mesoporous catalysts for HDPE hydrocracking

Microporous and Mesoporous Materials 356 (2023) 112605

Contents lists available at ScienceDirect

Microporous and Mesoporous Materials

journal homepage: www.elsevier.com/locate/micromeso

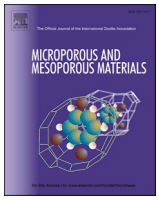

Evaluation of two approaches for the synthesis of hierarchical micro-/mesoporous catalysts for HDPE hydrocracking

Sabino Armenise [a], Catia S. Costa [b], Wong Syie Luing [c], M. Rosário Ribeiro [b], João M. Silva [d], Thomas Onfroy [e], Laetitia Valentin [e], Sandra Casale [e], Marta Muñoz [f,*], Franck Launay [e,**]

[a] CEPSA's Research Centre, Avenida Punto Com, 1, Alcalá de Henares, 28805, Madrid, Spain
[b] Centro de Química Estrutural, Institute of Molecular Sciences, Departamento de Engenharia Química, Instituto Superior Técnico, Universidade de Lisboa, Av. Rovisco Pais, 1049-001, Lisboa, Portugal
[c] Department of Chemical Engineering and Chemistry, Eindhoven University of Technology, P.O. Box 513, 5600, MB, Eindhoven, the Netherlands
[d] Instituto Superior de Engenharia de Lisboa, Instituto Politécnico de Lisboa, 1959-007, Lisboa, Portugal
[e] Laboratoire de Réactivité de Surface (LRS), UMR 7197 CNRS - Sorbonne Université, Campus Pierre et Marie Curie, 4 Place Jussieu, F-75005, Paris, France
[f] Departamento de Matemática Aplicada, Ciencia e Ingeniería de los Materiales y Tecnología Electrónica, Universidad Rey Juan Carlos, 28933, Madrid, Spain

ARTICLE INFO

Keywords:
Zeolite
Mesocellular foam
Nickel
HDPE hydrocracking
Hierarchy factor
Accessibility factor
Interplay factor

ABSTRACT

Plastic waste management has become a pressing global issue. A viable and sustainable alternative to incineration is the conversion of polyethylene into chemicals or fuels by through hydrocracking. To improve the catalytic performance during hydrocracking, bifunctional catalysts are required, in which the zeolite imparts the acid function, and the metallic function is provided by a noble or transition metal, such as nickel. In this study, acid supports were synthesized using two strategies, namely zeolitisation and desilication, for comparison. The synthesized materials exhibited Si/Al molar ratios of approximately 10, hierarchical micro-/mesoporosities, and a bifunctional character after incorporation of nickel up to 5 wt%. The materials were extensively characterized by various techniques, including powder X-Ray diffraction, N_2 sorption, acidity measurement, and scanning electron microscopy. The characterization results showed that the desilicated HZSM5 zeolite was the most effective support for nickel impregnation, leading to a quantitative conversion of High-Density Polyethylene (HDPE) by hydrocracking and the formation of predominantly hydrocarbons with 5 carbon atoms. A clear disparity in composition, with a prevalence of a gasoline-type fraction, was observable in the liquid phase from HZSM5 to Ni particles supported on hierarchical HZSM-5 (Ni@m-HZSM-5w). The hierarchy factor (HF), the molar ratio between Lewis and Brønsted acid sites, and the accessibility factor (ACI) were combined to form the interplay factor (IF). The investigation resulted in materials with IF values between 0.35 and 7, and a positive correlation between HDPE conversion and IF values is observed. In conclusion, this study suggests that the desilication of HZSM5 zeolite is a promising route for the development of efficient catalysts for the hydrocracking of plastic waste.

1. Introduction

From food packaging to aerospace applications, plastic has become a ubiquitous material in our daily life. However, due to the increased production and consumption of plastic along with the poor management, environmental pollution caused by plastic waste (PW) is becoming a real threat that requires immediate attention to protect the environment [1]. To develop a sustainable world, it is necessary to carefully take into account the waste management hierarchy [2]. The 6R's principle ("Reduce", "Repair", "Reuse", "Recover", "Remanufacturing'' and "Recycling") offers a framework for achieving the Sustainable Development Goals adopted by all the United Nations member states [3]. Although reducing is the key strategy to avoid incorporating more plastic into the environment, the American Chemistry Council pointed out that plastic production is far from being reduced, and forecasts that it will increase worldwide to 756 Mt by 2050 [4].

Despite the potential of recycling in minimizing energy and freshwater consumption, most post-consumer plastics cannot be used to

* Corresponding author.
** Corresponding author.
E-mail addresses: marta.munoz@urjc.es (M. Muñoz), franck.launay@sorbonne-universite.fr (F. Launay).

https://doi.org/10.1016/j.micromeso.2023.112605
Received 2 March 2023; Received in revised form 5 April 2023; Accepted 11 April 2023
Available online 15 April 2023

satisfy the same product needs; thus post-consumer plastics are often down-cycled [5]. Converting plastic waste into valuable chemicals or building block molecules through chemical routes is an efficient way to manage environmental concerns about plastic leaks and landfill disposal [6]. Among the thermochemical routes, thermal pyrolysis is by far the most commonly used one at semi-industrial and industrial scales [7,8]. However, several drawbacks remain to be overcome, such as a wide range of product distribution, significant coke formation and high energy inputs required to achieve full conversion of plastics feedstocks. Adding a catalyst (catalytic pyrolysis) results in a significant reduction of the reaction temperature and time, which provides better control over the hydrocarbon product distribution [9]. Nevertheless, the selectivity toward monomers, gasoline or diesel fraction remains low [10]. Additionally, the high coke yields together with the high aromatic and naphthene contents in the products obtained, even in the presence of catalysts, hinders the scale-up of catalytic pyrolysis. Detailed analyses of the state-of-the-art on these topics are provided in the literature [9, 11–15].

Hydrocracking (HDC) process is another promising pathway being considered for transforming PW into high-quality liquid fuels or building block molecules. HDC is considered by innumerable authors to be more advantageous than thermal and catalytic pyrolysis, as such process yields a highly saturated liquid product that can be directly used, without subsequent processing, as a transportation fuel or as fuel oil needed for power generation [16]. In addition, HDC occurs at lower temperatures than catalytic pyrolysis. Moreover, the presence of H_2 has beneficial effects both by removing heteroatoms (Cl, Br, F, etc.), and by giving extra lifetime to the catalyst through the reduction of coke deposition. The HDC reaction generally proceeds over a solid bifunctional catalyst, composed of an acid and a metallic source. The acid function is responsible for cracking and isomerization reactions, while the metal is responsible for hydro/dehydrogenation reactions [17]. Several types of bifunctional systems have already been tested for the conversion of plastic in a reducing atmosphere, namely, metal supported on zeolites (Pt/H-ZSM-5, Ni/H-ZSM-5, Pt/H-USY and Pt/H-Beta) [18–21], alumina and/or silica-alumina ($NiMo/Al_2O_3$, Pt/SiO_2, $NiMo/SiO_2–Al_2O_3$) [22–24] as well as solid superacid catalysts ($Pt/ZrO_2–SO_4$ and $Ni/ZrO_2–SO_4$) [25]. Most of the authors showed that catalyst features, especially the nature, number and strength of the acid sites and the pore size architecture, play crucial roles in the reaction [9]. Some authors termed to this close interaction, between metal particles and acid sites, as "site-intimacy", and is often related to better activities and performance in different bifunctional catalyzed reactions [26–28].

Maximizing the catalytic conversion and products selectivity through the design of hierarchical materials combining meso- and microporous properties has been a key step in improving a broad range of catalyzed reactions such as aromatization [29], alkylation [30], among others, and thermal valorization of various feedstocks, including biomass [31,32] and plastic wastes [33]. The micropore channels limit the reaction kinetics by diffusion phenomena. The occurrence of micropore channels and uncontrolled acidity can lead to undesirable over-cracking reactions, which in turn decrease the production of valuable products, and promote the deposition of coke. Bottom-up or top-down approaches have been pursued to synthesize hierarchical materials with superior catalytic properties, which are often directly related to acidity properties and pore accessibility [34]. Researchers are working to understand and establish meaningful relationships between surface area, acidity (number/strength) of the catalysts and their relative performance in order to develop a more rational design. Tarach et al. [35] are among the authors who took into account the accessibility of the acid sites, in order to understand the results obtained for the catalytic pyrolysis of Low-Density Polyethylene (LDPE). Using different probe molecules, Tarach et al. combined successfully the acidity strength factor (AS, measured by FTIR-pyridine), an accessibility factor (AF, determined by the ratio of pyridine and n-propylamine adsorption), and the hierarchy factor (HF, based on N_2 adsorption results, introduced earlier by Peréz-Ramiréz [36]), to link the activity of the catalysts with the intrinsic characteristics of the materials. Indeed, these authors were able to establish that those three co-dependent features (AS, AF and HF) control the performance of the catalyst, as shown by the straight lines that could be drawn between the conversion and the coupled parameters such as HF x AS or HF x AF.

The objective of the present paper was to design hierarchical materials through the partial conversion of alumino-silica mesocellular foams (MCF) into HZSM5 nano-crystallites at the surface of MCF ("zeolitisation"), which has not been reported before. The physicochemical and catalytic properties of those materials obtained by a "meso-to-microporous" approach were compared to those of a reference material arising from a controlled alkaline attack of HZSM5 ("micro-to-mesoporous" approach) with similar Si/Al ratio. Micro-to mesoporous (i) and meso-to microporous (ii) transformations were implemented in order to take advantage of the acidity, the interconnectivity and the pore size of mesoporous material for cracking processes and/or, HDC (after Ni incorporation) of High-Density Polyethylene (HDPE). Results are be discussed in the light of the intrinsic characteristics of the catalysts.

2. Materials and methods

2.1. Materials

The HDPE used in this work was supplied by Repsol. The polymer, without additives, was received in a powder form with a molecular weight (Mw) of 155,000 g/mol, a dispersity of 5.4 and a density of 0.95 g/cm^3. The HZSM5 zeolite used as parent material for hierarchical support preparation was acquired in ammonium form with a nominal Si/Al ratio of 11.5 from Zeolyst (CBV 2314). Sodium hydroxide (NaOH, 99 wt%), nitric acid solution (HNO_3, 65 wt%), Pluronic (P123), aluminum isopropoxide ($C_9H_{21}O_3Al$), trimethylbenzene (TMB), hydrochloric acid (HCl, 37 wt%), tetramethylorthosilicate (TMOS), tetrapropylammonium bromide (TPABr), ammonium fluoride (NH_4F) and the metal salt, nickel nitrate hexahydrate ($Ni(NO_3)_2.6H_2O$) from Sigma-Aldrich were used without further purification.

2.2. Catalyst preparation and characterization

2.2.1. "Micro-to-meso" approach (desilication)

The aim of this synthesis approach was to develop a microporous/mesoporous hierarchical structure through the modification of a preformed microporous zeolite in the protonic form (HZSM5). The hierarchical zeolite was obtained by a desilication process, employing base followed by acid treatments which was reported by Sartipi et al. [37].

First, the zeolite, in its ammonium form, was calcined at 500 °C for 5 h in a muffle furnace to obtain HZSM5 according to the method reported by Costa et al. [38]. Then, 10 g of HZSM5 were treated for 1 h with a solution of NaOH 1 M (8 mL/g of zeolite) at 70 °C under stirring at 500 RPM. The resulted suspension was quenched in an ice-water bath and centrifuged at 7000 RPM for 5 min to recover the solid part. The supernatant was separated, and the solid was washed thoroughly with distilled water in the centrifugation tube. Then, the modified zeolite was ion-exchanged 5 times with NH_4NO_3 0.2 M (50 mL/g of modified HZSM5) at room temperature to remove Na^+. After the last centrifugation, the solid recovered (m-NH_4ZSM5) was dried overnight at 60 °C followed by another 12 h at 120 °C and calcined at 550 °C for 5 h in a muffle furnace (0.5 °C/min) affording m-HZSM5. Finally, m-HZSM5 was treated with HNO_3 1 M (28.6 mL/g of m-HZSM5) at 70 °C for 2 h under stirring at 500 RPM to remove extra-framework aluminum (EFAl) species [39]. After quenching, using centrifugation, the recovered solid was washed 10 times with deionized water until a neutral pH was achieved, then dried, and calcined in a muffle furnace following the procedure mentioned above, affording m-HZSM5w.

2.2.2. "Meso-to-micro" approach ("zeolitisation")

The aim of this synthesis approach was to produce a microporous/mesoporous hierarchical support starting from a mesoporous material, here a mesocellular alumino-silica foam (Al-MCF). The hierarchical mesoporous material was prepared using controlled microwave heating of Al-MCF in the presence of fluorides and tetrapropylammonium bromide in order to partially convert amorphous alumina-silica at the surface into a HZSM5 deposit.

The Al-MCF was synthesized according to a protocol adapted from the work of Daoura et al. [40], and considering a TMB/P123 wt ratio of 4, as described by Al-Naji et al. [41]. First, "solution A" was prepared as follows: 4 g of Pluronic P123 were dissolved under stirring at 40 °C in 150 mL of HCl aqueous solution at pH = 1.5. After 2 h, 16 g of TMB was added dropwise into the mixture under 1000 RPM stirring in order to get a microemulsion. The mixture was left stirring overnight. In parallel, "solution B" was prepared at room temperature by the slow introduction (over 4 h) of 6.4 mL TMOS and 0.8 g aluminium isopropoxide to 10 mL of a HCl aqueous solution at pH = 1.5 affording a theoretical Si/Al ratio of 11.5. Finally, "solution B" was added to "solution A" and the resulting blend was kept at 40 °C for 24 h under the same stirring rate. After that, 48 mg of NH_4F was added and stirred for 5 min. Finally, the suspension was transferred into a Teflon bottle and treated hydrothermally in an oven at 100 °C for 24 h. Then, the synthesized material was separated by vacuum filtration and washed abundantly with distilled water, dried at 60 °C for 15 h and calcined in a muffle furnace at 550 °C for 6 h (heating rate 1 °C min^{-1}).

"Zeolitisation" of Al-MCF was performed using a method developed by Habib et al. [42] with adaptation as follows: firstly, the parent Al-MCF (2.7 g) was impregnated by a solution made of 4 g of TPABr in 17 mL of distilled water. The impregnated solid was kept under magnetic stirring for 1 h followed by water removal. Then, water was evaporated until dryness using a rotavapor equipment. The solid recovered was further dried overnight at 60 °C. The solid, thus obtained, was suspended in 54 mL of distilled water, and the pH was adjusted to 10 with 0.1 M NaOH. Later, the content of the resulting suspension was transferred into 4 Teflon reactors and placed in an Anton Paar Synthos 3000 multimode microwave oven. "Zeolitisation" was performed either at 180 °C, 500 W for 4.5 h (Al-MCF_{Z1}) or at 200 °C, 1200 W for 4.5 h (Al-MCF_{Z2}). After completing the reaction time and subsequent quenching, the sample was filtered and rinsed with deionized water for several times. Then, the material was ion-exchanged with NH_4NO_3 to replace Na^+ by NH_4^+, and finally dried and calcined as mentioned early in "micro-to-meso" approach.

2.2.3. Metal incorporation

Nickel(II) from an aqueous solution of $Ni(NO_3)_2.6H_2O$ was incorporated within Al-MCF_{Zx} and m-HZSM5w supports using incipient wetness impregnation. Hence, the volume of water used to dissolve Ni $(NO_3)_2.6H_2O$ was equal to the total pore volume of m-HZSM5(w) or Al-MCF ($_{Z1}$ or $_{Z2}$). In both cases, the aqueous solution of Ni(II) (0.247 g_{Ni_salt}/g_{sup}) was added dropwise under mechanical stirring. Then, the recovered greenish materials were air-dried at 60 °C during 24 h and calcined at 500 °C under airflow of (4×10^3 mL/h·g STP). Before being used, all the impregnated catalysts were reduced under hydrogen flow of (4×10^3 mL/h·g STP) for 2 h, at 500 °C. All the metal-based catalysts were prepared with a theoretical Ni content of 5 wt% and identified throughout the work as Ni@m-HZSM5w and Ni@Al-MCF($_{Z1}$ or $_{Z2}$) for m-HZSM5w and Al-MCF($_{Z1}$ or $_{Z2}$) supports, respectively.

2.3. Catalysts characterization

The textural properties of the parent support and the synthesized materials were characterized by N_2 physisorption technique using a Micromeritics TRISTAR 3000 instrument at −196 °C. Samples were outgassed under high vacuum at 350 °C for 24 h prior to analysis to remove any physisorbed species. The BET surface areas (S_{BET}) were determined through the application of the Brunauer, Emmett and Teller equation [43]. Mesoporous surface area (S_{Meso}) was determined according to the method described in Ref. [36]. The micropore volume (V_{micro}) was calculated using the t-plot method [44], while the total pore volume (V_{total}) was determined from the adsorbed volume of nitrogen at a relative pressure, P/P_o = 0.99. The mesopore volume (V_{Meso}) was obtained by the difference between V_{Total} and V_{Micro}. The pore size distribution was determined using the BJH-method.

The structures of the parent supports and the synthesized materials were evaluated by Powder X-Ray diffraction (PXRD). PXRD analysis was performed on a Bruker AXS D8 diffractometer operating at 30 kV and 30 mA, using Cu K_α radiation (α = 1.541 Å) as X-ray source. For low-angles, the data were collected in the 2θ range from 0.5° to 5° with a step of 0.02° and a counting time of 6 s/step. Wavelength-dispersive X-ray fluorescence spectrometry (WDXRF) was used to determine Ni, Al and Si contents in the samples. The equipment used was an Axios FAST (PANalytical Zetium), where the source of radiation was Rh K_α and data was analyzed by SuperQ software. The acid properties of the samples were analyzed by monitoring pyridine adsorption/desorption by Fourier-transform infrared spectroscopy (FTIR). Before analysis, thin discs of samples (4–11 mg/cm^2) were prepared by compacting powder at ~1 tons/cm^2. Before pyridine adsorption/desorption experiments, the wafers were treated under oxygen (260 mbar) at 450 °C (ramp: 2 °C/min) for 30 min and then outgassed under a secondary vacuum at 450 °C for 30 min. Wafers were then contacted with gaseous pyridine (approximately 1.33 mbar) at 150 °C for 15–30 min to allow sufficient diffusion of the probe molecules into micropores. The spectra were then recorded following a desorption step of 30 min from 150 to 450 °C with a Bruker Vector 22 spectrometer (resolution 4 cm^{-1}, 64 scans). The reported spectra were obtained after subtraction of the spectrum recorded before pyridine adsorption and normalization at 10 mg/cm^2. The amount of Brönsted and Lewis acid sites (BAS and LAS) titrated by pyridine was obtained using the molar absorption coefficient values of ε = 1.09 and 1.76 cm/μmol for the ν_{19b} vibration of protonated (Py-B) at ~1545 cm^{-1} and coordinated pyridine (Py-L) at ~1450 cm^{-1}, respectively [45]. In order to determine the accessibility of the BAS by specific probe molecules, temperature-programmed decomposition (TPD) of n-propylamine was performed in a TGA/DSC thermal analyzer (model: SDT Q600, TA Instruments). In a regular procedure, n-propylamine was added to the dried samples, then the samples were degassed at 150 °C for 10 min to remove the physisorbed n-propylamine molecules. After that, the samples were heated under flowing nitrogen (30 mL/min) at temperatures of 150–700 °C with a heating rate of 10 °C/min. From the amount of acid sites, detect by IR or by TPD, accessibility indexes have been calculated using the following equations:

$$ACI_{pyr} = \frac{C_m(BAS) + C_m(LAS)}{C_m(Al)} \text{ and } ACI_{n-pro} = \frac{C_m(n-propylamine)}{C_m(Al)} \quad \text{(Equation 1)}$$

with C_m(BAS) and C_m(LAS) the weight concentration of Brönsted and Lewis acid sites obtained from pyridine desorption at 150 °C, C_m(Al) the weight concentration of aluminum in the solid and C_m(n-Propylamine) the weight concentration of amine adsorbed. From these two values, the Accessibility Factor have also been calculated as follows:

$$ACI_{pyr} = \frac{ACI_{pyr}}{ACI_{n-pro}} x\ 100 \quad \text{(Equation 2)}$$

Morphological analyses via Field Emission Gun Scanning Electron Microscopy (FEG-SEM, Hitachi) were conducted using an acceleration voltage of 1 kV and an emission current of 64000 nA for mesocellular foams. Meanwhile, a Scanning Electron Microscope (FEGSEM Nano-Nova 230 FEI) was used for zeolite materials with an acceleration voltage of 3–5 kV. Transmission Electron Microscopy (TEM) images were acquired at 100 kV using a JEOL 1011 instrument equipped with a Gatan camera (3-Å resolution). Prior to the measurements, the materials

were dispersed in ethanol with ultrasounds and a drop was deposited on a copper grid covered by a thin film of carbon. Theoretical metal dispersion was measured following the procedure reported by Bond [46], considering the nickel content reported by XRF and the particle size from TEM analysis.

2.4. Hydrocracking (HDC) catalytic tests

The samples used for the hydrocracking experiments were prepared using a compression molding. The HDPE and catalyst, both in powder form, were mechanically mixed with a polymer-to-catalyst mass ratio of 80/20, and then heated in a molding press at 140 °C and under 3 tons of pressure for 5 min.

The HDC tests were carried out in a 100 mL batch autoclave reactor from Autoclave Engineering equipped with a magnetic stirrer, as described in a work by Ref. [47]. The reactor was heated by an electric furnace connected to a programmable temperature controller. The temperature of the furnace was controlled via three K-type thermocouples at three different zones of the furnace (upper, middle, and bottom). Additionally, the temperature of the reaction zone was monitored by a J-type thermocouple, placed in the reactor. The gas pressure in the reactor was measured by a pressure gauge. The reactor was filled with 1 g of the sample, then the reactor was purged thrice with N_2 to remove oxygen from the reactor. Subsequently, the reactor was pressurized with 20 bar of hydrogen (H_2) at room temperature and heated (1.5 °C/min) until 260 °C for 1 h, for the reaction to take place. The mass of gaseous products formed during the reaction was determined after GC analysis considering the total volume of gases discharged. The remaining products were recovered from the reactor and extracted with hexane in order to remove the liquid fraction formed during the reaction. The solid fraction, composed of the unconverted plastic, catalyst, and coke, was dried overnight at 60 °C to evaporate the solvent. The yields of gas and liquid products and the conversion of the process were determined according to the following equations:

$$Conversion\ (\%) = \frac{m_{HDPE} - m_{unconverted\ HDPE}}{m_{HDPE}}\ x\ 100 \quad \text{(Equation 3)}$$

$$Gas\ yield\ (wt.\%) = \frac{m_{Gas}}{m_{HDPE}}\ x\ 100 \quad \text{(Equation 4)}$$

$$Liquid\ yield\ (wt.\%) = \frac{m_{products\ soluble\ in\ hexane}}{m_{HDPE}}\ x\ 100 \quad \text{(Equation 5)}$$

where m_{HDPE} and $m_{unconverted\ HDPE}$ are the weight of HDPE (g) used in the experiment and the weight of HDPE (g) remaining in the reactor after the reaction, respectively; m_{Gas} (g) is the weight of total gasses product collected. In all experiments performed, the mass balance was closed with a range of 94–100%.

2.5. Products characterization

The composition of the gaseous fraction was analyzed by gas chromatography (GC) equipped with a flame ionization detector (GC-FID) using a GC1000 DPC chromatograph and a capillary HP-PONA column (50 m × 0.2 mm x 0.5 mm) from Agilent. This analysis allows separation and identification of the gaseous components in terms of carbon atom number. The liquid products were characterized by a simulated distillation analyzer according to the ASTM D 2887 method. The system consists of a Hewlett Packard 5890 gas chromatography equipped with a FID detector and a DB-2887 capillary column (10 × 0.53 mm x 0.3 mm) from Agilent. This procedure allows separation of the liquid hydrocarbons in the function of their boiling points. The solid fraction resulting from the HDC reaction was analyzed through two thermogravimetric analysis (TGA) cycles using a Setaram TGA-92 apparatus, in order to quantify the amount of unconverted HDPE as well as the carbon deposit over the catalyst. First, 20 mg of the solid sample containing unreacted plastic, coke, and the catalyst was heated to 500 °C at a heating rate of 10 °C/min and held for 1 h under nitrogen flow (30 mL/min), to remove unreacted HDPE from the remaining components of the solid fraction. The sample obtained from the first TGA cycle, consisting of coke and catalyst, was then heated to 800 °C at a rate of 10 °C/min and held for 30 min in an air atmosphere (30 mL/min) to burn off all the coke deposited over the catalytic system. The amount of unreacted HDPE was determined by the difference between the final and the initial mass of the sample in the first TGA cycle, while the amount of coke was determined by the mass difference obtained from the second TGA cycle.

3. Results and discussion

This section starts with a description on the evolution of the physicochemical properties of the starting materials (with Si/Al ≫ 10) toward materials with hierarchical porosity is proposed. This was done for HZSM5 and Al-MCF that were used, respectively, for the synthesis of m-HZSM5$_W$ and Ni@m-HZSM5$_W$ ("micro-to-meso" approach) as well as Al-MCF$_{Z1}$, Al-MCF$_{Z2}$, Ni@Al-MCF$_{Z1}$ and Ni@Al-MCF$_{Z2}$ ("meso-to-micro" approach). The implemented protocols are derived from the literature. The m-HZSM5w support was obtained by desilication in basic medium, followed by acid treatment to remove EFAl species as described by Sartipi [37]. The Al-MCF$_{Z1}$ and Al-MCF$_{Z2}$ supports were synthesized via treatment of the mesoporous alumino-silica under controlled hydrothermal conditions, using microwave, in basic medium and in the presence of the templating agent of ZSM5 [38]. In the latter case, two types of "zeolitisation" conditions were applied (Z1: 180 °C, 500 W and Z2: 200 °C, 1200 W). For both series, nickel was introduced up to 5 wt% (4.5 wt% for Ni@m-HZSM5$_W$ and Ni@Al-MCF$_{Z1}$, 4.3 wt% for Ni@Al-MCF$_{Z2}$). In both cases, analyses were used to characterize the acidity, the accessibility of the acid sites as well as the porosity hierarchization. These data were then used to explain the results of the catalytic tests during the cracking of HDPE under reducing conditions.

3.1. Catalysts characterization

Fig. 1 shows the N_2 sorption isotherms of the starting materials used for the "micro-to-meso" and "meso-to-micro" approaches as well as those of the synthesized materials with or without Ni. Textural properties of the materials are provided in Table 1. As expected for microporous materials, parent HZSM5 zeolite, with a MFI-structure, is characterized by a plateau at low relative pressure (type-I shape according to IUPAC). However, after desilication and acid washing steps on m-HZSM5w, the shape of the adsorption/desorption isotherms changed from type-I to type-IV isotherms corresponding to materials bearing both micro- and mesopores. A remarkable hysteresis loop starting from $P/P_0 = 0.42$ suggests the presence of occluded or partially isolated mesopores [44]. Consequently, an increase of mesopore area and volume of 68 and 92% respectively, was evidenced (Table 1). Meanwhile, almost no change in the surface and volume of the micropores could be detected. As previously reported by Yang et al. [48], zeolite desilication processes lead to mesoporous structure formation by partial destruction of micropores walls. As shown in Table 1, S_{Meso}/S_{BET} ratio increased from 24% to 35% and V_{Meso}/V_{Total} from 48% to 69% (calculated from the data in Table 1 as 100-V_{Micro}/V_{Total}).

In their work, Tarach et al. [35] observed the negative effect of alkaline treatment on the micropore volume. However, the results obtained in our study indicate only a slight change. Fig. 1 shows that such treatment is responsible for the formation of a new, broad pore size distribution centered around 20 nm. The impact of the desilication process on the hierarchical features of the attacked materials has been described early by a set of contributions from Verboekend and Pérez-Ramírez [47]. Those authors introduced the hierarchy factor (HF, equation (6)) whose calculation takes in account the formation of the mesopores as well as the preservation of the micropore volume.

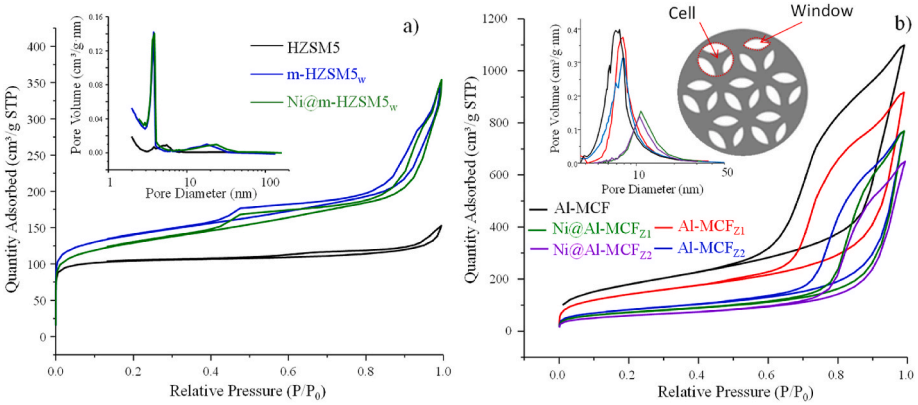

Fig. 1. N_2 adsorption-desorption isotherms of hierarchical materials with or without Ni as well as their parents for a) "micro-to-meso" and b) "meso-to-micro" approaches. Insets in each graph display the pore size distribution obtained from desorption branches (BJH model).

Table 1
Textural parameters of starting materials and their hierarchical derivatives with or without Ni based on N_2-sorption measurements.

Material	Surface Area (m^2/g)				Pore Volume (cm^3/g)			HF [36] [c]
	S_{BET}	S_{Meso} [a]	S_{micro} [a]	S_{Meso}/S_{BET}	V_{tot} [b]	V_{micro}	V_{micro}/V_{tot}	
Zeolites								
HZSM5 (CVB 2314)	411	97	313	0.24	0.25	0.13	0.52	0.12
m-HZSM5$_W$	470	163	307	0.35	0.36	0.13	0.36	0.13
Ni@m-HZSM5$_W$	425	225	200	0.53	0.45	0.14	0.31	0.16
Mesocellular Foams								
Al-MCF	512	512	0	1.00	1.02	0.00	0.00	0.000
Al-MCF$_{Z1}$	498	455	22	0.91	1.12	0.01	0.01	0.009
Al-MCF$_{Z2}$	216	186	30	0.86	1.13	0.01	0.01	0.008
Ni@Al-MCF$_{Z1}$	288	268	0	0.93	1.12	0.01	0.01	0.007
Ni@Al-MCF$_{Z2}$	210	190	0	0.90	1.12	0.01	0.01	0.006

[a] t-plot method applied to N_2 adsorption isotherm.
[b] Calculated at $P/P_0 = 0.99$.
[c] HF has been calculated according to reference [46] (equation (6)). For Ni samples the analysis was performed under oxidized form.

$$HF = \left(\frac{V_{micro}}{V_{total}}\right) * \left(\frac{S_{meso}}{S_{BET}}\right) \quad \text{(Equation 6)}$$

where V_{micro} and V_{total} are the volumes of the micropores only and of all types of pores respectively, while S_{meso} and S_{BET} are the surface area of the mesopores, and all types of internal and external surfaces measured by the BET method. All of them are calculated using N_2 adsorption/desorption data. In the present work, the "micro-to-meso" approach based on a desilication process led to a slight increase of HF (from 0.12 to 0.13) compared to the parent material. Nickel addition increased the HF to a slightly higher value (0.16) which indicates Ni is not blocking the pore entrance, which is consistent with well-dispersed metal particles on the surface. These values are in agreement with those obtained in early works by Verboekend et al. [49–51] for HZSM5 zeolite.

The N_2 sorption isotherms of the alumino-silica mesocellular foam, Al-MCF (Fig. 1b), used as starting material in the "meso-to-micro" approach are typical, especially the wide hysteresis loop for $0.5 < P/P_0 < 1.0$. The average values for the cell (D_{cell}) and window (D_{win}) diameters, estimated by the BJH method applied to the adsorption and desorption branches, were $D_{cell} = 20$ and $D_{win} = 9$ nm, respectively. Based on the results displayed in Table 1, "zeolitisation" process performed under the mildest conditions, 180 °C and 500 W, (Al-MCF$_{Z1}$) had almost no impact on the textural properties of the parent Al-MCF. It was thus decided to strengthen the conditions (higher temperature and power (200 °C and 1200 W)). The resulting material, Al-MCF$_{Z2}$, was characterized by a substantial decrease in the surface area (50%) and a sharp increase of the average value of D_{win} (14 nm), probably associated with a partial collapse of the pore walls as a consequence of the "hot-spots" generation by microwave irradiation, as reported by Wang et al. [52]. However, in the two sets of "zeolitisation" conditions employed here, no significant differences were observed for the micropores volumes and surfaces compared to Al-MCF were obtained. The values of HF were about 20 times less than those of the materials prepared by the "micro-to-meso" approach.

Ni incorporation into m-HZSM5$_W$ and Al-MCF$_{Z2}$ materials led to some decreases in the micropore surface area. The total pore volume was almost unmodified for mesocellular foams, but it increased by 25% after the incorporation of Ni in m-HZSM5$_W$.

Fig. 2 displays the PXRD patterns of the different materials. Classical diffraction peaks characteristic of the MFI structure could be highlighted for all samples used in the "micro-to-meso" approach (Fig. 2a). It is could be estimated that ca. 60% of the crystallinity was maintained after desilication as shown by the comparison of the intensity of the peak at 2° - 23° for m-HZSM5$_W$ and HZSM5 (Fig. 2a shows different scale bars). Samples loaded with Ni revealed, after calcination, the presence of NiO species with diffraction peaks at $2\theta = 37.17°$, 43.25°, 62.74°, 75.46° and 79.13° corresponding to the (111), (200), (220), (311), (222) lattice planes expected for face-centered cubic NiO (JCPDS 89–7130).

As expected, Al-MCF is an amorphous alumino-silica. Its PXRD diffraction patterns showed only a broad peak for $18° < 2\theta < 38°$, resulting from X-ray scattering. (Fig. 2b). After "zeolitisation" (Z1 and Z2 conditions), no peaks corresponding to HZSM5 could be observed, but NiO species could be evidenced in the case of calcined Ni@Al-MCF$_{Z1}$ and Ni@Al-MCF$_{Z2}$. After the reduction procedure, only the peaks corresponding to Ni^0 species ($2\theta = 44.6°$, 52.00° and 76.35°) were detected (Fig. S1), indicating that all Ni particles were in the reduced form for the

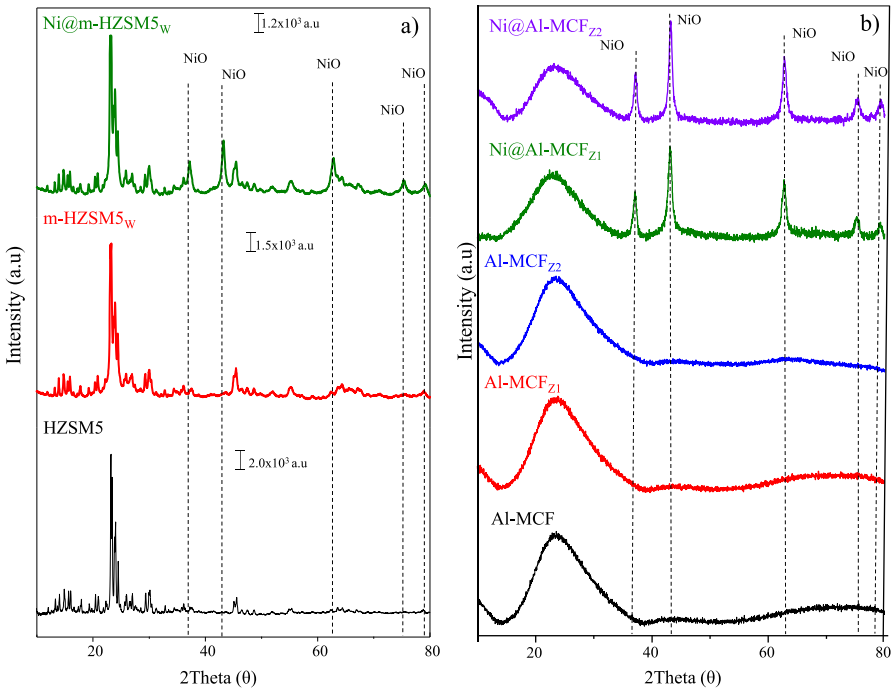

Fig. 2. XRD patterns of hierarchical materials with or without Ni as well as their parents for a) "micro-to-meso" and b) "meso-to-micro" approaches. XRD analysis of Ni samples was carried out on the oxidized form. Different scale bars are displayed in "Fig. 2a" to compare the intensity between PXRD patterns.

catalysis tests. The average size of NiO crystallites in Ni@Al-MCF$_{Z1}$ and Ni@Al-MCF$_{Z2}$ were estimated using the Scherrer equation to be in the range of 8–14 nm. Such values are compatible with the deposition of Ni particles inside the porosity and not only on the outer surface. It should be noted that the average value of the size of Ni oxide crystallites estimated by PXRD for Ni@m-HZSM5$_W$ was lower (about 8 nm).

The impacts of the desilication and "zeolitisation" treatments over the morphological properties of HZSM5 and Al-MCF, respectively have been investigated by SEM and TEM analysis of the Ni-free solids. In the series of HZSM5-based materials (Fig. 3a–b), the main 2D morphology

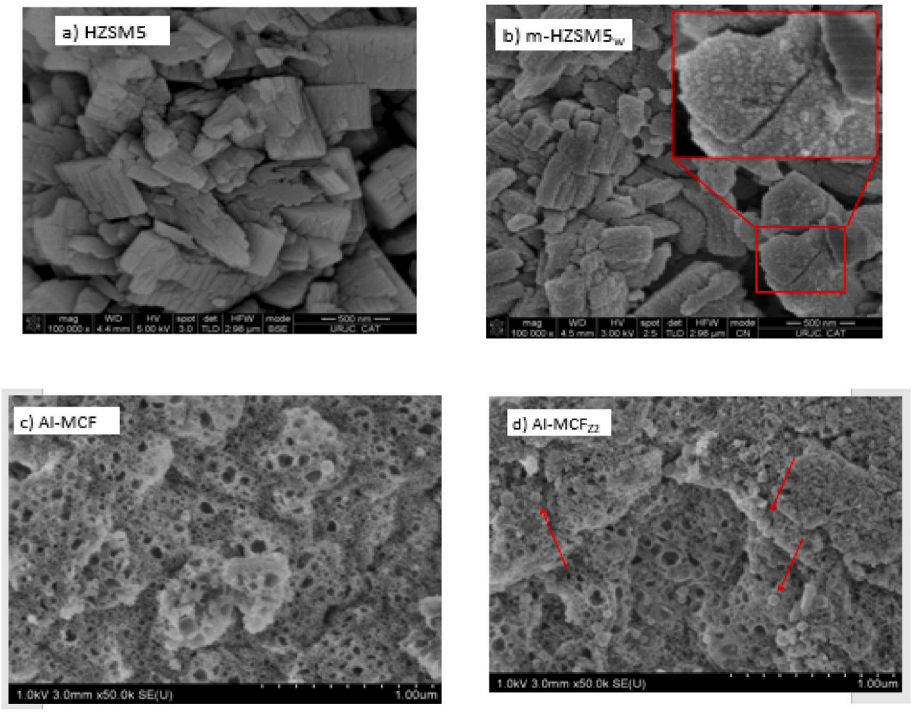

Fig. 3. Scanning electron microscopy images of a) HZSM5; b) HZSM5 after desilication and acid treatment; c) parent Al-MCF, and d) Al-MCF$_{Z2}$. Magnification of certain regions shows a detailed view of the impact of the treatments employed. Al-MCF did not show any appreciable change of morphology after the treatment used to get Al-MCF$_{Z1}$.

was maintained. The only difference was a homogeneous modification in the surface roughness of the zeolite after the desilication process. In the series of Al-MCF materials (Fig. 3c–d), the parent support showed a typical morphology for classical foams structure with, apparently, 3D interconnected channels with a regular, qualitatively, bi-modal distribution of "pore-mouth". After the most aggressive "zeolitisation" conditions ("Z2"), an apparent increase in the roughness of the external surface was also observed. The formation of additional small particles (indicated by red arrows in Fig. 3d) probably indicates the nucleation of solid parts at the expense of the mesocellular framework, following an increase in the hardness of the "zeolitisation" conditions.

TEM analysis on the parent zeolite used in the "micro-to-meso" approach (Fig. 4a) revealed crystals with homogeneous sizes of ca. 0.15 × 0.9 μm and a HZSM5 structure characterized by an interplanar distance of 1.11 nm, as reported by Wu et al. [53] (Fig. S2). After desilication, intra-crystalline mesopores appear to be present by the observation of lighter areas within the crystals. (Fig. 4b).

TEM analysis of Al-MCF evidenced a very fragmented and porous material with patterns similar to those reported previously [54]. As expected, the material recovered after "zeolitisation" under the mildest conditions, Al-MCF$_{Z1}$, did not appear to be very different (Fig. 4d). Alternatively, images of the sample prepared under the hardest "zeolitisation" conditions, Al-MCF$_{Z2}$ (Fig. 4e), were quite different. Indeed, Al-MCF$_{Z2}$ did not appear to be as homogeneous as Al-MCF$_{Z1}$. Instead, Al-MCF$_{Z2}$ looks like a combination of a typical-opened mesocellular foam and a denser solid structure, indicating probably inadequate distribution of the heating during microwave irradiation treatment. In a previous study of our group [55], the optimization of conditions for partially converting another mesoporous alumino-silica (Al-SBA-15) into HZSM5 under microwave irradiation was successful. However, it seems that these optimized conditions are not applicable to Al-MCF. Based on the findings in this study, it is concluded that the "meso--to-micro" pathway is much more difficult to control compared to the "micro-to-meso" one. Previous work on "zeolitisation" performed by other groups emphasized that a non-uniform distribution of heat/energy inside the reactor vessel under microwave irradiation may strongly affect zeolite crystallization [56]. In this work, the porosity of Al-MCFZ1 and Al-MCFZ2 is still dominated by mesopores since the hierarchy factors reached (Table 1) are too low (ca. 0.01) [57].

Fig. 5 shows the results of the TEM analysis of the materials recovered after Ni deposition and before the reduction step. Similar to m-HZSM5$_W$, Ni@m-HZSM5$_W$ (Fig. 5a) was characterized by the presence of cavities (clear domains) generated during the desilication treatment (Fig. 4b). Apparently, Ni incorporation in m-HZSM5$_W$ did not obstruct the porosity. NiO nanoparticles were found to have a small average diameter, i.e. about 4 nm (indicated by red arrows), which is consistent with the pore size distribution established by BET analysis, thus confirming the possibility for nickel ions to diffuse into the pores network of the zeolite hierarchical structure. In addition, other nanoparticles with diameters lower than 1 nm located probably inside the micropores channel of the zeolite are detected. Particle sizes much larger than those reported for Ni@m-HZSM5 were revealed on the TEM images of Ni@Al-MCF$_{Z1}$ and Ni@Al-MCF$_{Z2}$ (Fig. 5b and c). The average dimensions for these materials were about 9.5 and 9.0 nm, respectively, which is consistent with the above-mentioned PXRD results. Here, it seems that the cells (*ca.* 14 nm) of Al-MCF exert an influence on the Ni particle size.

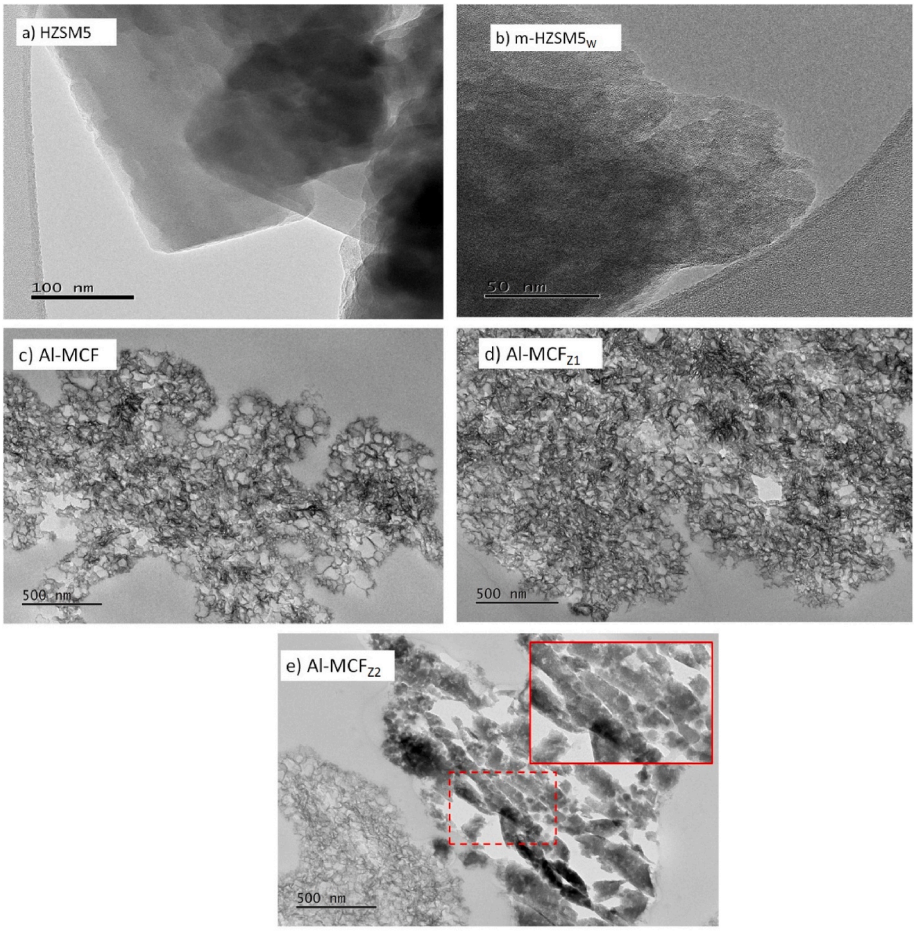

Fig. 4. Transmission electron microscopy images of a) parent zeolite; b) zeolite after desilication/acid treatment; c) parent Al-MCF, d) Al-MCF$_{Z1}$, e) Al-MCF$_{Z2}$. (c, d and e images were obtained by microtomy).

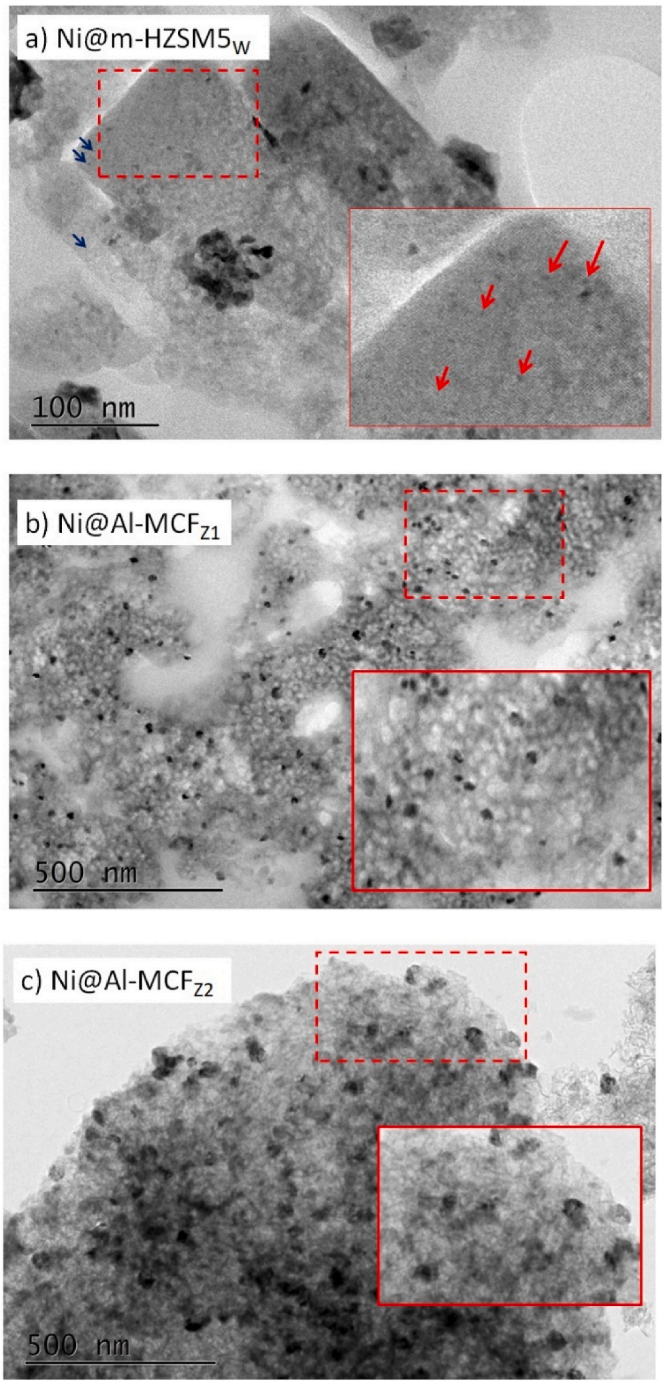

Fig. 5. Transmission electron microscopy images of the Ni-impregnated catalysts: a) Ni@m-HZSM5$_W$; b) Ni@Al-MCF$_{Z1}$ and c) Ni@Al-MCF$_{Z2}$. TEM images for Ni sample were collected on the oxidized form.

Fig. 6a–b shows the characteristic FTIR spectra of the different materials after pyridine desorption at 150 °C. All the samples based on HZSM5 or Al-MCF present six typical bands between 1400 and 1700 cm^{-1}. The two bands at 1634 cm^{-1} and 1545 cm^{-1} are attributed to the ν_{8a} and ν_{19b} vibration modes of pyridinium ions associated with Brønsted acid sites (BAS). The bands at 1622 cm^{-1} and 1611 cm^{-1} are characteristics of the ν_{8a} vibration mode of coordinated pyridine on the strongest and weakest Lewis acid sites (LAS), respectively. The band at 1455 cm^{-1} is related to the ν_{19b} vibration mode of coordinated pyridine. Meanwhile, the band at 1489 cm^{-1} is attributed to the ν_{19a} vibration mode of coordinated and/or protonated pyridine.

Alkaline and acid treatments on HZSM5 led to a decrease in the intensity of the characteristic bands of BAS (1545 cm^{-1}). On the contrary, a substantial increase in the band's intensity attributed to the strongest LAS (1622 cm^{-1}) was observed, probably as an indication of the creation of defects or the presence of EFAl [58]. Ni introduction also reduce the intensity of the band characteristic of BAS (1545 cm^{-1}). This was accompanied with a significant increase in the intensity of the band associated with weak LAS (1612 cm^{-1}). In parallel, the band assigned to coordinated pyridine (1455 cm^{-1}) became the most intense part of the FTIR spectrum. However, the "zeolitisation" of Al-MCF to Al-MCF$_{Z1/Z2}$ led to almost no change in the FTIR spectrum, thus corroborating the low efficiency of such post-treatment in the present contribution. It must be noted that the band's intensity attributed to strong LAS (1623 cm^{-1}) is already predominant in the spectrum of Al-MCF, while it was not for the H-ZSM5 series. Later, especially after Ni introduction, strong Lewis acid sites seemed to be replaced by weak LAS (1611 cm^{-1}) as already mentioned for Ni@m-HZSM5$_W$.

According to the data shown in Table 2, the HZSM5 precursor is characterized by a rather high concentration of BAS (625 μmol/g), and a large fraction of these sites were shown to be strong, able to retain one-third of pyridine up to 350 °C (Fig. S3.1). LAS were also present in HZSM-5, but to a lower extent (60 μmol/g) which is mostly related to the presence of EFAl species [59]. The desilication process followed by acid washing led to a strong decrease of the concentration of BAS sites concentration (from 625 to 128 μmol/g), while LAS concentration significantly strongly increased (from 60 to 148 μmol/g), with almost no change of the Si/Al ratio. It seems that about one LAS is formed through the disappearance of about five BAS, which is in agreement with earlier results reported by Holm et al. [60]. Alkaline etching is known to be highly selective towards silicon, but, in this work, the washing step, which is used to extract aluminum atoms, was not accompanied by their reinsertion, in line with previous results reported by Milina et al. [61].

Despite a similar Si/Al ratio, the mesocellular alumino-silica foam, as well as its derivatives, were characterized by a much lower concentration of acid sites, especially of the BAS, compared to the materials obtained from H-ZSM5. Regardless of the "zeolitisation" procedure applied, the resulting samples displayed ca. 20 μmol/g of BAS, instead of 45 for the Al-MCF precursor. Additionally, all the BAS turned out to possess low acidic strength, as they could not retain pyridine at 250 °C. Importantly, all samples, including Al-MCF, presented a higher concentration of LAS compared to BAS (approximately 2-fold). Moreover, all materials showed strong LAS, able to retain pyridine at temperatures up to 450 °C (Fig. S3.2).

As mentioned above, the integration of Ni into m-HZSM5$_W$ has also strongly modified its acid properties. Re-oxidation of Ni(0) in Ni@m-HZSM5w either into NiO or Ni^{2+} with concomitant formation of H^+ or H_2O, under the air treatment performed before FTIR measurements, is very likely to happen. This is the reason why it could be observed that Ni incorporation led to a decrease in the BAS concentration from 128 μmol/g to 64 μmol/g, revealing the replacement of BAS protons by Ni^{2+} exchangeable cations [62] or some pore blocking by NiO. In parallel, expectedly, the Ni introduction induced an increase of the LAS by approximately 65% (from 148 μmol/g to 207 μmol/g). Such behaviour was reported previously by our team during the incorporation of Ni over SiBEA and HAlBEA and is associated with Ni species acting like Lewis acids [38]. Trends were not so clear after Ni introduction onto Al-MCF$_{Z1}$ and Al-MCF$_{Z2}$.

As summarized in Fig. 7a, a significant increase in the mesopores surface area at the expense of the BAS concentration was achieved by the "micro-to-meso" approach. LAS became dominant but the overall acidity was divided by 2.5, resulting in a Ni-based catalyst with 64 mmol/g of BAS, 207 mmol/g of LAS and 225 m^2/g of mesopore surface area. With 16–27 mmol/g of BAS, 46–101 mmol/g of LAS and 190–268 m^2/g of mesopore surface area, Ni-based catalysts (Ni@Al-MCFz$_1$ and Ni@Al-MCFz$_2$) from the "meso-to-micro" approach were not significantly different from Ni@HZSM5$_W$. Results show that "zeolitisation" led to a

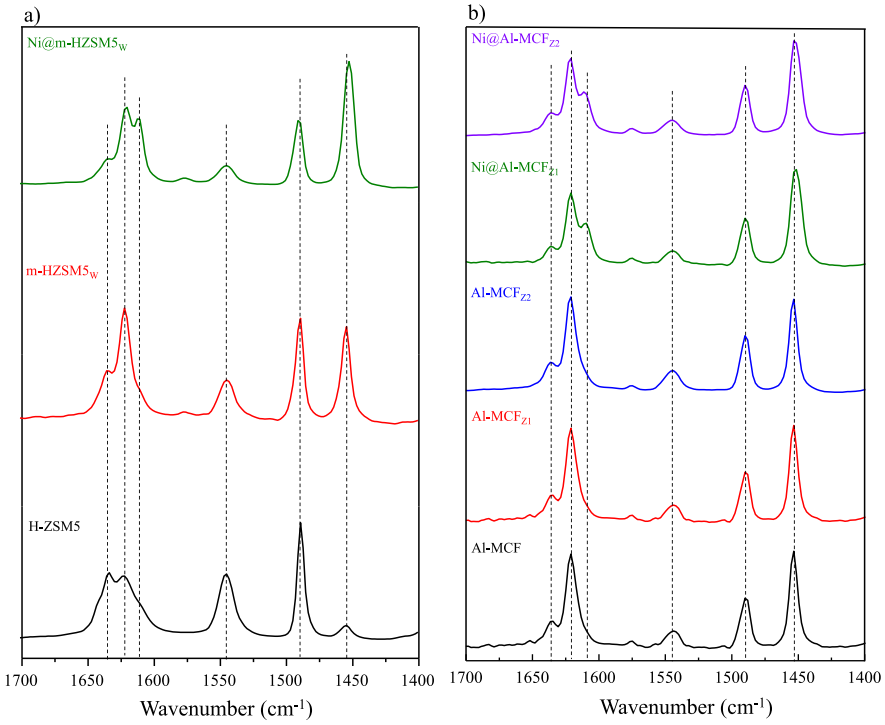

Fig. 6. Representative FTIR spectra of pyridine desorption at 150 °C for hierarchical materials with or without Ni as well as their parents for a) "micro-to-meso" and b) "meso-to-micro" approaches. FT-IR was measured after Ni reduction. The reported spectra were obtained after subtraction of the spectrum recorded before pyridine adsorption and normalization at 10 mg/cm^2.

Table 2
Physicochemical characterization of the catalysts employed on hydrocracking.

Material	Si/Al ratio[a]	Al content [μmol/g cat][a]	Acid site quantification								
			Pyridine adsorption [b] [μmol/g cat]								
			Brønsted C_B		**Lewis C_L**		**L/B Ratio, AS**	**n-Propylamine decomposition, $C_{n\text{-}pro}$, [μmol/g cat]**	**ACI_{Pyr}[c]**	**$ACI_{n\text{-}pro}$[d]**	**AF (%)[e]**
			150 °C	**250 °C**	**150 °C**	**250 °C**					
Zeolites											
HZSM5	10.8	1557	625	482	60	46	0.1	1701	0.44	1.09	40.2
m-HZSM5$_W$	11.0	1408	128	71	148	103	1.2	1898	0.20	1.35	14.5
Ni@m-HZSM5$_W$ (4.5)[f]	11.1	1400	64	32	207	145	3.2	1855	0.19	1.33	14.6
Mesocellular Foams											
Al-MCF	9.9	1668	42	nd	95	56	2.3	635	0.08	0.38	21.6
Al-MCF$_{Z1}$	6.1	2361	20	nd	45	28	2.3	365	0.03	0.15	17.8
Al-MCF$_{Z2}$	6.2	2339	25	nd	47	31	1.9	257	0.03	0.11	28.0
Ni@Al-MCF$_{Z1}$ (4.5)[f]	7.7	1783	27	nd	101	60	3.7	524	0.07	0.29	32.0
Ni@Al-MCF$_{Z2}$ (4.3)[f]	6.6	2157	16	nd	46	25	2.9	332	0.03	0.16	17.6

[a] Measured by X-ray fluorescence.
[b] Measured by quantitative experiments of pyridine desorption at different temperatures.
[c] ACI_{Pyr} = Ratio between the amount of Brønsted (C_B) + Lewis (C_L) sites determined by pyridine at 150 °C and the amount of aluminum in the samples.
[d] $ACI_{n\text{-}pro}$ = Ratio between $C_{n\text{-}pro}$ and the amount of aluminum in the samples. nd = non-detected.
[e] Ratio between the amount of ($C_B + C_L$) measured by pyridine at 150 °C and the amount of n-propylamine measured by TPD ($ACI_{Pyr}/ACI_{n\text{-}pro}$).[f] Concentration of Ni measured by X-ray fluorescence.

twofold decrease in the overall acidity keeping the distribution of BAS and LAS almost constant (Fig. 7b). Indeed, it seemed to have little impact on the development of BAS and micropores. Last but not least, the smaller sizes of the Ni particles measured on Ni@m-HZSM5$_W$, compared to Ni@Al-MCF$_{Z1}$ and Ni@Al-MCF$_{Z2}$ materials, is in good correlation with the population of BAS, as suggested earlier by Wang et al. [63].

In heterogeneous acid catalysis, the reaction kinetics can be limited by the diffusion to and from active sites. In order to understand catalysis results, especially for hierarchical supports, the definition of an accessibility index (ACI) was shown to be useful. Pérez-Ramírez et al. [61] defined such an index as the number of acid sites detected by the probe

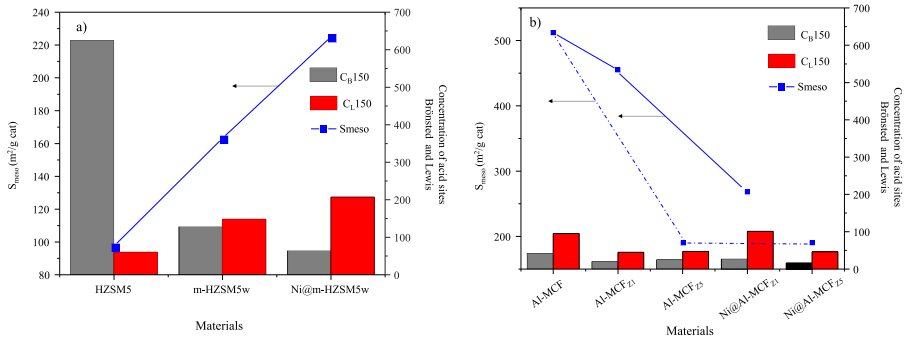

Fig. 7. Correlation between the amount of Brønsted (BAS) and Lewis (LAS) acid sites (bars), and mesopore surface area S_{meso} (continued and dotted line, for Z_1 and Z_2 samples, respectively). BAS or LAS were calculated as the amount of acid sites measured by pyridine desorption at 150 °C (C_B *or* C_L) for hierarchical materials with or without Ni as well as their parents for a) "micro-to-meso" and b) "meso-to-micro" approaches.

molecule divided by the total amount of Al in the material.

Table 2 displays the accessibility indexes for pyridine desorption (ACI_{Pyr}). For Al-MCF, the ACI_{Pyr} value turned out to be very low while it was about 0.44 for HZSM-5. Pyridine has a kinetic diameter of 0.57 nm. In the case of the HZSM5 series, it is possible that part of the micropores was blocked, thus limiting the access of pyridine to the acid sites. Corma et al. [64] also demonstrated by computational simulation that pyridine itself may hinder the adsorption of other pyridine molecules due to its steric bulkiness. It is worth highlighting that, after the desilication step followed with the acid treatment, the uptake of pyridine did not increase. In fact, the ACI_{Pyr} decreased despite the increase of the mesopore surface area. Such results must be related to structures isolation or the lack of interconnectivity within the microporous framework, making these acid sites "partially inaccessible" for pyridine molecules knowing that a similar explanation has been suggested by Holm et al. [60].

To clarify such a hypothesis, the adsorption-decomposition of n-alkylamine was used to determine the accessibility of Brønsted sites to probe molecules with a lower kinetic diameter. Indeed, the application of the temperature-programmed decomposition of reactive amines with different kinetic diameters is an alternative to evaluate the accessibility of the acid sites. Parrillo et al. [65] were the first to propose alkylamine adsorption for the stoichiometric determination of BAS. Although there was some controversies regarding the interpretation of the acid strength obtained from these analyses, due to problems of re-adsorption and diffusion [66,67], temperature-programed desorption or temperature-programed decomposition of n-alkylamines is considered to give a good estimate of the acid side density of a sample. In this work, n-propylamine (ca. 0.52 nm) decomposition was used to allow the determination of another accessibility index, $ACI_{n\text{-}pro}$. Whatever the material considered, the use of n-propylamine allowed systematic detection of more acid sites than pyridine. According to the data displayed in Table 2, $ACI_{n\text{-}pro}$ for parent HZSM5 showed a value of 1.09, which is close to the value reported by Parrillo et al. [65] for HZSM5. Considering this, $ACI_{n\text{-}pro}$ should remain constant after desilication since Si/Al ratio did not change. However, a slight rise of the $ACI_{n\text{-}pro}$ was observed in our case. Such discrepancy has been observed previously [65] and was associated with the defects in the zeolite structure originating from incomplete or deficient Al reintegration into the zeolite framework.

To summarize, the differences emphasized by the use of the two probe molecules tested on the materials from the "micro-to-meso" approach, with the increase of mesopores surface areas, indicate the presence of acid sites accessible to n-propylamine, which seem to be located in partially isolated mesopores regions that cannot be reached by a bulkier molecule such as pyridine [66]. This is supported by: i) the reduction of crystallinity observed after desilication (measured by XRD) as well as ii) the reduction of the intensity of the pyridine absorption band detected at 1545 cm^{-1} (measured by FTIR).

Due to its amorphous nature, Al-MCF was characterized by much lower values of $ACI_{n\text{-}pro}$ and ACI_{Pyr} than HZSM5. In fact, all its derivatives obtained by the "meso-to-micro" approach verified this trend (ACI_{Pyr} and $ACI_{n\text{-}pro}$ values < 0.08 and 0.38, respectively). In this series dominated by mesopores, it proved to be difficult to highlight an appreciable change of the accessibility of the acid sites.

Fig. 8 shows IR spectra of hydroxyl groups of all the materials before and after desilication/"zeolitisation" treatments. The parent HZSM5 was the only one presenting a very intense band at 3609 cm^{-1} related to the bridged OH groups in Si(OH)Al at the origin of its strong Brønsted acidity, and mostly associated with the stretching mode of extra-framework H^+ [27,67,68,69]. The second band, by order of intensity, at 3743 cm^{-1}, is usually attributed to isolated Si–OH groups. Finally, at 3658 cm^{-1}, a third band is attributed to Al–OH of EFAl. m-$HZSM5_W$ was also characterized by the same three bands, but desilication has induced a strong decrease in the amount of bridged –OH groups evidenced by the loss of intensity of the band at 3609 cm^{-1} (ca. 80% compared to the parent zeolite). Additionally, it induced the creation of a large number of silanol groups. Indeed, the band's intensity at 3743 cm^{-1} is four times higher than that for the parent HZSM5. Finally, the comparison of the spectra of treated and non-treated zeolites shows the creation of EFAl

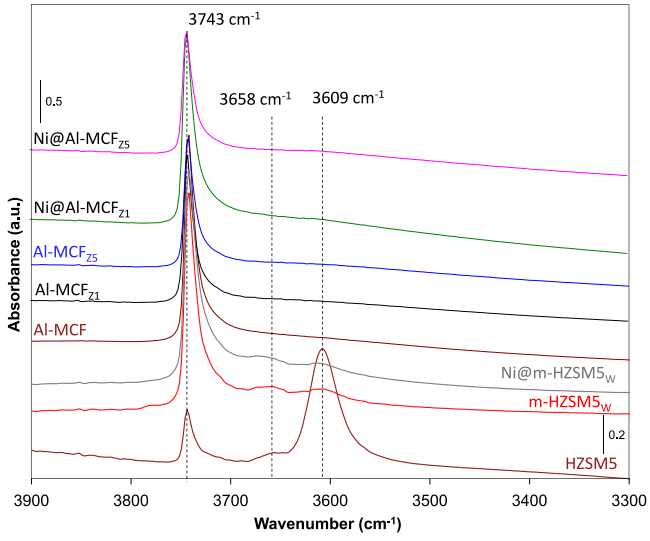

Fig. 8. IR spectra (normalized at 10 mg/cm^2 of pellets) of the hydroxyl region of hierarchical materials with or without Ni as well as their parents for "micro-to-meso" and "meso-to-micro" approaches. (Recorded at room temperature after thermal treatment at 450 °C for 0.5 h under 200 Torr of O_2 and 0.5 h under secondary vacuum). Profile of the Al-MCF and its derivatives were multiplied by 2.5.

characterized by the band at 3658 cm^{-1} which increased two-fold compared to the parent zeolite. This observation agrees with the pyridine desorption results monitored by FTIR. Incorporation of Ni into m-$HZSM5_W$ did not induce strong modifications of the spectrum in this region. However, a decrease of the amount of bridged OH groups could be evidenced by the loss of intensity of the band at 3609 cm^{-1} (approx. -50%) that could be related to H^+ exchange.

Al-MCF and the materials derived from "zeolitisation" were also characterized by a very intense band at 3743 cm^{-1}. According to the literature [70], this band corresponds to Si–OH groups in a weak interaction with an aluminum atom, giving rise to a lower acid character than that in HZSM5. The "zeolitisation" process seems to have a non-negligible effect on the amount of these OH groups (divided by 2 for Al-MCF_{Z2}), in agreement with the acidity measurements done by pyridine adsorption. However, regardless of the "zeolitisation" treatment, a band at ca. 3610 cm^{-1}, which is characteristic of Si(OH)Al (BAS of HZSM5), was not detected. "Zeolitisation" under microwave radiation only modified the Al–Si framework without significant formation of zeolite. Ni incorporation decreased the number of OH groups by 5%, compared to the "zeolitized" Al-MCF support. However, this variation is relatively weak and should be considered with caution as it is close to the measurement accuracy.

4. Catalytic test

The catalytic activities of the prepared materials by the "micro-to-meso" and "meso-to-micro" approaches were tested, before and after Ni impregnation process, with the HDPE hydrocracking reaction at 260 °C for 60 min, under 20 bar of H_2 and using 20 wt% of catalyst. The trend presented in Fig. 9a has been organized according to increasing HDPE conversions, showing that "zeolitized" materials, including the corresponding Ni-based catalysts, are less active than HZSM5 itself and the materials resulting from its desilication. The HDPE conversion in the presence of the hierarchical zeolite, m$HZSM5_W$ increased by 20% compared to the pristine zeolite, changing from 67% to 87%. The incorporation of Ni onto m$HZSM5_W$ also induced a positive effect on the overall performance of the catalyst, resulting in the full conversion of HDPE. Such performances are superior to those previously reported by our team for a Ni@HZSM5 zeolite tested under the same conditions [Conversion = 95%, Yield in gas = 89.7 wt%, Yield in liquid = 4.9 wt%].

In this work, as suggested by Pérez-Ramírez [61,71] and in agreement with Tarach et al., the hierarchy (HF) and accessibility (AF) factors of the different materials have been merged and associated with the acidity strength (AS or L/B), measured as the Lewis/Brønsted ratio, giving rise to the Interplay Factor (IF), which has benn calculated as follows:

$$IF = HF\ x\ AF\ x\ AS \qquad \text{(Equation 7)}$$

Fig. 9a also displays the IF values, hence showing that IF and HDPE conversions follow similar trends. This "apparent" dependence reveals that Lewis acidity (AS) and the hierarchical structure (HF) have a strong impact on the catalyst's performance (Fig. 9b), which is in agreement with the work of Tarach. More analyses, e.g. operando characterization techniques, would be required to draw further conclusions. Tuning the acidity strength and the accessibility of the active sites by increasing the mesoporosity without substantial loss of micropore surface area seems to be the best strategy to achieve the desired catalytic performance. The higher conversion of HDPE reached in the presence of the hierarchical zeolite compared to the parent one could correspond to the lowered diffusion path and the transformation of the strongest Brønsted acid sites into moderate ones, as shown by n-propylamine analysis. Considering the large increase of LAS and the sharp decline of BAS recorded after desilication in this work, it is unlikely that the superior performance of the hierarchical zeolite, m-$HZSM5_W$, would be related to the increase of the Brønsted acidity due to some synergism or charge transfer of Brønsted sites with Lewis sites [72,73]. In our opinion, the higher content of aluminum atoms located in extra-framework position in m-$HZSM5_W$ may contribute to increase the adsorption/interaction of HDPE molecules with OH groups near to the Al atoms in the framework and improve the conversion of HDPE, as suggested earlier by Brunner et al. in the catalytic cracking of hexane over dealuminated HZSM5 [74].

No reaction occurred with Ni@Al-MCF_{Z1} and Ni@Al-MCF_{Z2} under the reaction conditions applied, presumably due to their low content of BAS (Table 2) which results in a low propensity to induce the activation of C–C bonds cleavage [72]. In our case, the low microporosity gained after the "zeolitisation" process was lost probably due to some pore blocking. Our results show strong evidence that a compromise between micro-mesoporosity, hierarchical accessibility and acid strength is needed in order to properly guide the design of more efficient catalysts.

The effect of the acidity tuning could be highlighted through the product yield distribution between the gas, liquid and solid phases (Fig. 10a) as well as the distribution of the resulting hydrocarbons in the gaseous (C_1 to C_5) (Fig. 10b) and liquid (C_6 to C_{13+}) (Fig. 10c–d) products. Mesocellular foams recovered after "zeolitisation" led to a higher yield of solids (char) than the other catalysts. Moreover, it has to be noted that, considering the low number of acid sites present in these materials and the high H_2-pressure conditions, solids recovered at the end of those tests, done in the absence of Ni, should correspond to mainly non-reacted HDPE. The non-appreciable variation of the textural or acidity properties, including HF, AF and AS, between Al-MCF_{Z1} and Al-MCF_{Z2} would explain why the yields of liquids and gasses are practically the same for both samples (Fig. 10a). The results obtained with the Ni incorporation into the catalysts, show that Ni@Al-MCF_{Z1} and Ni@Al-MCF_{Z2} were not better catalysts. It seems then that the structural and textural parameters listed above are the determining features, instead of the average size of the Ni particles, which was almost the same for the hierarchical zeolite (effective catalyst) and mesocellular foams (ineffective catalyst). Looking back to the values of mesopore surface

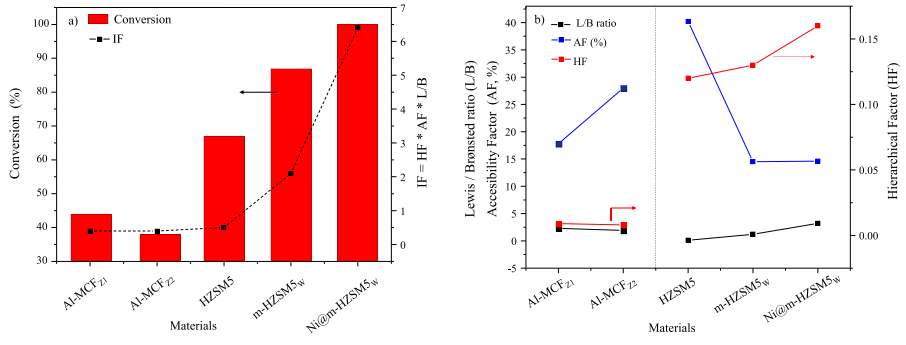

Fig. 9. a) Correlation plot between the Interplay Factor (IF) of the solids and the HDPE conversion; b) Evolution of L/B, HF and AF. For the sake of clarity. Ni@Al-MCF_{Z1}, Ni@Al-MCF_{Z2} and Al-MCF samples were removed due to their low activity. (Conditions: 260 °C for 60 min under 20 bar of H_2, using 20 wt% of catalyst).

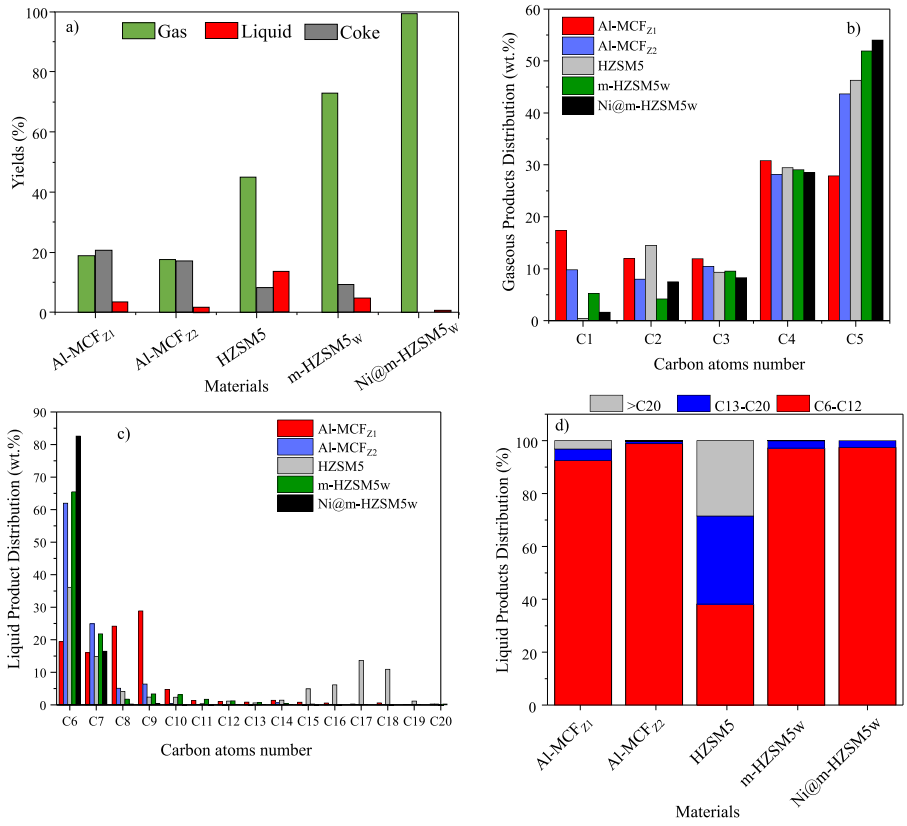

Fig. 10. HDPE hydrocracking over Al-MCF (Z1 and Z2), HZSM5, m-HZSM5w and Ni@m-HZSM5w (Conditions: 260 °C for 60 min under 20 bar of H_2, using 20 wt% of catalyst). a) Product yield distribution between the gas, liquid and solid phases; b) Gaseous products distribution by carbon atom number; (c) (d) Liquid products distribution by carbon atom number and by fractions, respectively.

area and acidity, the low catalytic performance could be related to the loss of microporosity after nickel deposition by pore-blocking phenomena, and poor acidity characteristics (in absolute terms). Several authors have pointed out that cracking of linear alkanes over Brønsted acid sites occurs via protonation to give carbonium ions, leading to much faster reactions than hydride ion abstraction over Lewis acid sites [73]. This also explains the limited conversion of HDPE in the presence of the mesocellular foam and its derivatives characterized by the lowest Brønsted sites concentration.

Even though HZSM5, the parent zeolite, was characterized by the highest number of BAS, its activity turned out to be lower than that of its hierarchical counterpart, m-HZSM5$_W$. On one hand, BAS in the zeolite micropores are the location for highly selective catalytic reactions but they fail to affect molecules that are larger than the pore size. On the other hand, small pore sizes and long diffusion path lengths reduce transport efficiency and cause poor catalyst utilization and thus decrease the catalytic rates. Clearly, the long polymer chains of HDPE cannot fit easily to the small openings of the HZSM5, being cracked on strong BAS of the external surface. To decrease the likelihood of over-cracking reactions and subsequent coke formation, the loss of BAS can be controlled through by (i) reducing their acid strength or converting them into LAS, and (ii) creating a hierarchical structure by performing desilication. Moreover, it could be observed that the yields of liquid decreased from HZSM5 to m-HZSM5$_W$, thus highlighting the formation of hydrocarbon fractions with shorter chains. This could be explained by the promotion of hydrogen transfer reactions by LAS, as reported by Muller et al. [75] and Istadi et al. [76].

Slight differences in hydrocarbon distributions in both liquid and gaseous phases obtained from HDC of HDPE could be observed, as shown in Fig. 10a. Systems based on HZSM5 (with the highest conversions of HDPE) led mainly to gaseous products and especially to C_5 hydrocarbons, whose percentage increased from 46 to 51% after desilication and to 54% after Ni deposition. The distribution of C_1–C_4 hydrocarbons for such systems decreased with the increase of HDPE conversion, i.e. with the development of mesoporosity (see HF values in Table 1) and the diminution of the Brønsted acidity. The presence of lower hydrocarbon gases compounds is associated mainly with an end-chain cracking mechanism, typical of a microporous (zeolite) structure [77,78], which decreased from HZSM5 to mHZSM5w as the result of the generation of mesopores by desilication. Similar distribution was reported by Ding et al., who studied the HDC of HDPE over MFI-type zeolites [79]. There is a relationship between the pore size of the catalysts and the tendency to form lighter hydrocarbons [80,81]. Almost 100% gaseous products were produced with Ni@m-HZSM5$_w$ but with no significant changes for the hydrocarbon composition was observed upon Ni incorporation.

Recent works on the hydrocracking reaction of LDPE over HY (30) and HZSM5 catalysts showed that the product distribution can be pore shape-sensitive [82–84]. Large pore catalysts were shown to be able to provide a higher yield of gasoline-range hydrocarbons, meanwhile microporous catalysts led to the formation of C_1–C_4 hydrocarbons. For all the materials in the series of the zeolite-based catalysts, the fraction of C_1–C_4 showed similar trends (Fig. 10b). However, the C_5 fraction increased with the L/B ratio (see Table 2) indicating the contribution of LAS in the promotion of gaseous products with heavier molecular weights. Similar findings have been extensively reported in the literature. In comparison with HZSM5-derived solids, Al-MCF-based catalysts led to a wider distribution of the products in the gas phase. Considering the low concentration of BAS and large pore size of these mesocellular foams, a gas products distribution more oriented towards heavier molecular weights (C_4–C_5) was expected, but this trend was not followed.

Regarding the product distribution in the liquid phase, HZSM5 was

characterized by the lowest selectivity for the production of the gasoline fraction (C_6–C_{12}) relative to the diesel one (C_{13}+) which turned out to be absent with all the other catalysts (Fig. 10c). HZSM5 desilication (m-HZSM5w) led to a tremendous change of selectivity with 98% of gasoline (Fig. 10d). Ni impregnation (Ni@m-HZSM5w) led almost exclusively to C_6 and C_7 products. However, it is important to point out that the liquid yield obtained over Ni@m-HZSM5w corresponds to a very small part of the products obtained (3 wt%). Both Al-MCF_{Z1} and Al-MCF_{Z5} also led to a liquid product distribution centered on the gasoline range, exhibiting a selectivity higher than 90%.

5. Conclusion

Two synthetic methods, based either on a "micro-to-meso" or a "meso-to-micro" approach starting from HZSM5 and Al-MCF, respectively, afforded micro/mesoporous hierarchical materials with *ca.* Si/Al = 10 and HF values ranging from 0.006 to 0.16.

The microwave-assisted “zeolitisation” attempts on Al-MCF revealed low efficiency for the partial conversion of Al-MCF into HZSM5 deposits (very low HF values of *c.a.* 0.006) and, as the result, a rather low content of Brønsted and Lewis acid sites, leading to IF values lower than 1. On the other hand, desilication of HZSM5 led to a significant improvement of IF (values higher than 1) as a result of i) the significant development of mesopores, without decreasing too much the micropores, and to a lower extent, ii) the increase of the Lewis acid content.

The corresponding solids impregnated or not with Ni (*ca.* 5 wt%) were tested by the hydrocracking reaction of HDPE, thus emphasizing a clear correlation between the HDPE conversion and the Interplay Factor, especially the Hierarchical Factor and the Lewis/Brønsted acid sites ratio. The relatively high proportion of Lewis acid sites in the Al-MCF materials is not decisive on its own since most of the solids prepared in this work, including the best-performing ones in HDC processes, were characterized by Lewis/Brønsted values of the order of 3; neither was the accessibility factor (comparison of the interaction with two bases of different sizes, here pyridine and n-propylamine).

The solids obtained from the desilication of HZSM5 were found to be the most active in HDC, leading to more than 80% conversion of HDPE to gaseous products (C_1–C_5 fraction). The introduction of Ni enabled 100% conversion while suppressing coke formation. Furthermore, it was found that, among the gaseous products generated, more C_5 compounds seem to be produced at the expense of compounds containing between 1 and 4 carbon atoms for the materials characterized by the highest IF values. Interestingly, on the liquid phase product side, the desilication of the zeolite led to a significant improvement of the selectivity for the gasoline fraction at the expense of the diesel fraction. However, it should be noted that the liquid phase is almost negligible especially when Ni is added.

To conclude, this study highlights the desilication method of HZSM5 which involves different synthesis parameters (NaOH concentration, duration of the attack, quantity introduced, size of the zeolite crystals) that need to be optimized in order to improve the IF value and, who knows, the performance of the materials obtained regarding HDC.

CRediT authorship contribution statement

Sabino Armenise: Writing – original draft, Methodology, Investigation, Formal analysis, Conceptualization. **Catia S. Costa:** Investigation. **Wong Syie Luing:** Writing – review & editing, Visualization. **M. Rosário Ribeiro:** Investigation, Conceptualization. **João M. Silva:** Investigation, Conceptualization. **Thomas Onfroy:** Validation, Investigation. **Laetitia Valentin:** Validation, Investigation. **Sandra Casale:** Investigation. **Marta Muñoz:** Writing – review & editing, Supervision, Funding acquisition. **Franck Launay:** Writing – review & editing, Supervision, Formal analysis.

Declaration of competing interest

The authors declare that they have no known competing financial interests or personal relationships that could have appeared to influence the work reported in this paper.

Data availability

Data will be made available on request.

Acknowledgements

Dr. Sabino Armenise and Dr. Wong Syie Luing, have received support from the European Union’s Horizon 2020 research and innovation programme under the Marie Skłodowska-Curie grant Agreement No. 754382, GOT ENERGY TALENT. Dr. Armenise want to dedicate special thanks to Sorbonne University and to all research department of Cepsa who help to characterize the catalysts and to C. Prieto, J. Frontela, B. Aramburu and R. Larraz to support this postdoctoral research. This research has been carried out during the postdoctoral position at URJC-CEPSA. Funding from Fundação para a Ciência e Tecnologia, Project UIDB/00100/2020, Project UIDP/00100/2020 and Project LA/P/0056/2020 is also gratefully acknowledge. The publication is part of the TED2021-129688B project, funded by MCIN/AEI/10.13039/501100011033 and by the European Union "NextGenerationEU"/PRTR. The content of this publication does not reflect the official opinion of the European Union. Responsibility for the information and views expressed in this paper lies entirely with the authors.

Appendix A. Supplementary data

Supplementary data to this article can be found online at https://doi.org/10.1016/j.micromeso.2023.112605.

References

[1] J. Jenna, M. Ellie, D. Brajesh, Leveraging Multi-Target Strategies to Address Plastic Pollution in the Context of an Already Stressed Ocean, OceanPanel, 2020. https://www.oceanpanel.org/blue-papers/leveraging-target-strategies-to-address-plastic-pollution-in-the-context. (Accessed 6 January 2022).
[2] M. Gharfalkar, R. Court, C. Campbell, Z. Ali, G. Hillier, Analysis of waste hierarchy in the European waste directive 2008/98/EC, Waste Manag. 39 (2015) 305–313, https://doi.org/10.1016/j.wasman.2015.02.007.
[3] J. Kirchherr, D. Reike, M. Hekkert, Conceptualizing the circular economy: an analysis of 114 definitions, Resour. Conserv. Recycl. 127 (2017) 221–232, https://doi.org/10.1016/j.resconrec.2017.09.005.
[4] R. Geyer, J.R. Jambeck, K.L. Law, Production, use, and fate of all plastics ever made, Sci. Adv. 3 (2017), e1700782, https://doi.org/10.1126/sciadv.1700782.
[5] I. Vollmer, M.J.F. Jenks, M.C.P. Roelands, R.J. White, T. Harmelen, P. Wild, et al., Beyond mechanical recycling: giving new life to plastic waste, Angew. Chem. Int. Ed. 59 (2020) 15402–15423, https://doi.org/10.1002/anie.201915651.
[6] A.J. Martín, C. Mondelli, S.D. Jaydev, J. Pérez-Ramírez, Catalytic processing of plastic waste on the rise, Chem (2021), https://doi.org/10.1016/j.chempr.2020.12.006.
[7] S.L. Wong, S. Armenise, B.B. Nyakuma, A. Bogush, S. Towers, C.H. Lee, et al., Plastic pyrolysis over HZSM-5 zeolite and fluid catalytic cracking catalyst under ultra-fast heating, J. Anal. Appl. Pyrolysis 169 (2023), 105793, https://doi.org/10.1016/j.jaap.2022.105793.
[8] L. Paula, D. Kate, B. Croke, G. Sherwin, B. Miñana, ACCELERATING CIRCULAR SUPPLY CHAINS FOR PLASTICS: A LANDSCAPE OF TRANSFORMATIONAL TECHNOLOGIES THAT STOP PLASTIC WASTE, KEEP MATERIALS IN PLAY AND GROW MARKETS, 2020. https://www.closedlooppartners.com/.
[9] D.P. Serrano, J. Aguado, J.M. Escola, Developing advanced catalysts for the conversion of polyolefinic waste plastics into fuels and chemicals, ACS Catal. 2 (2012) 1924, https://doi.org/10.1021/cs3003403. –41.
[10] P.T. Williams, E. Slaney, Analysis of products from the pyrolysis and liquefaction of single plastics and waste plastic mixtures, Resour. Conserv. Recycl. 51 (2007) 754–769, https://doi.org/10.1016/j.resconrec.2006.12.002.
[11] M. Solis, S. Silveira, Technologies for chemical recycling of household plastics – a technical review and TRL assessment, Waste Manag. 105 (2020) 128–138, https://doi.org/10.1016/j.wasman.2020.01.038.
[12] S. Armenise, S. Wong, J.M. Ramírez-Velásquez, F. Launay, D. Wuebben, B. B. Nyakuma, et al., Application of computational approach in plastic pyrolysis kinetic modelling: a review, React. Kinet. Mech. Catal. 134 (2021) 591–614, https://doi.org/10.1007/s11144-021-02093-7.

[13] S.L. Wong, N. Ngadi, T.A.T. Abdullah, I.M. Inuwa, Current state and future prospects of plastic waste as source of fuel: a review, Renew. Sustain. Energy Rev. 50 (2015) 1167–1180, https://doi.org/10.1016/j.rser.2015.04.063.
[14] S.M.M. Al-Salem, A. Antelava, A. Constantinou, G. Manos, A. Dutta, A review on thermal and catalytic pyrolysis of plastic solid waste (PSW), J. Environ. Manag. 197 (2017) 177–198, https://doi.org/10.1016/j.jenvman.2017.03.084.
[15] H. Hernando, A.M. Hernández-Giménez, C. Ochoa-Hernández, P.C.A. Bruijnincx, K. Houben, M. Baldus, et al., Engineering the acidity and accessibility of the zeolite ZSM-5 for efficient bio-oil upgrading in catalytic pyrolysis of lignocellulose, Green Chem. 20 (2018) 3499–3511, https://doi.org/10.1039/c8gc01722k.
[16] D. Munir, M.F. Irfan, M.R. Usman, Hydrocracking of virgin and waste plastics: a detailed review, Renew. Sustain. Energy Rev. 90 (2018) 490–515, https://doi.org/10.1016/j.rser.2018.03.034.
[17] A. Kostyniuk, D. Bajec, B. Likozar, Hydrocracking, hydrogenation and isomerization of model biomass tar in a packed bed reactor over bimetallic NiMo zeolite catalysts: tailoring structure/acidity, Appl. Catal. Gen. 612 (2021), 118004, https://doi.org/10.1016/j.apcata.2021.118004.
[18] N.D. Hesse, R.L. White, Polyethylene catalytic hydrocracking by PtHZSM-5, PtHY, and PtHMCM-41, J. Appl. Polym. Sci. 92 (2004) 1293–1301, https://doi.org/10.1002/app.20083.
[19] Z. Pan, X. Xue, C. Zhang, D. Wang, Y. Xie, R. Zhang, Production of aromatic hydrocarbons by hydro-liquefaction of high-density polyethylene (HDPE) over Ni/HZSM-5, J. Anal. Appl. Pyrolysis 136 (2018) 208–214, https://doi.org/10.1016/j.jaap.2018.10.004.
[20] C.S. Costa, M. Muñoz, M.R. Ribeiro, J.M. Silva, V. Gatard, D. De Masi, et al., A thermogravimetric study of HDPE conversion under a reductive atmosphere, Catal. Today (2020), https://doi.org/10.1016/j.cattod.2020.07.021.
[21] J.A. Salbidegoitia, E.G. Fuentes, M.P. González-Marcos, J.R. González-Velasco, Recycle of plastic residues in cellular phones through catalytic hydrocracking to liquid fuels, J. Mater. Cycles Waste Manag. 19 (2017) 782–793, https://doi.org/10.1007/s10163-016-0478-z.
[22] J. Mosio-Mosiewski, M. Warzala, I. Morawski, T. Dobrzanski, High-pressure catalytic and thermal cracking of polyethylene, Fuel Process. Technol. 88 (2007) 359–364, https://doi.org/10.1016/j.fuproc.2006.10.009.
[23] A. Tennakoon, X. Wu, A.L. Paterson, S. Patnaik, Y. Pei, A.M. LaPointe, et al., Catalytic upcycling of high-density polyethylene via a processive mechanism, Nat Catal 3 (2020) 893–901, https://doi.org/10.1038/s41929-020-00519-4.
[24] K.S. Rothenberger, A.V. Cugini, R.L. Thompson, M.V. Ciocco, Investigation of first-stage liquefaction of coal with model plastic waste mixtures, Energy Fuel. 11 (1997) 849–855, https://doi.org/10.1021/ef9602077.
[25] K.R. Venkatesh, J. Hu, W. Wang, G.D. Holder, J.W. Tierney, I. Wender, Hydrocracking and hydroisomerization of long-chain alkanes and polyolefins over metal-promoted anion-modified zirconium oxides, Energy Fuel. 10 (1996) 1163–1170, https://doi.org/10.1021/ef960049j.
[26] J. Zecevic, G. Vanbutsele, K.P. de Jong, J.A. Martens, Nanoscale intimacy in bifunctional catalysts for selective conversion of hydrocarbons, Nature 528 (2015) 245–248, https://doi.org/10.1038/nature16173.
[27] E. Gutierrez-Acebo, C. Leroux, C. Chizallet, Y. Schuurman, C. Bouchy, Metal/acid bifunctional catalysis and intimacy criterion for ethylcyclohexane hydroconversion: when proximity does not matter, ACS Catal. 8 (2018) 6035–6046, https://doi.org/10.1021/acscatal.8b00633.
[28] J. Harmel, L.I. van der Wal, J. Zečević, P.E. de Jongh, K.P. de Jong, Influence of intimacy for metal-mesoporous solid acids catalysts for n -alkanes hydroconversion, Catal. Sci. Technol. 10 (2020) 2111–2119, https://doi.org/10.1039/C9CY02510C.
[29] Y. Li, S. Liu, Z. Zhang, S. Xie, X. Zhu, L. Xu, Aromatization and isomerization of 1-hexene over alkali-treated HZSM-5 zeolites: improved reaction stability, Appl. Catal. Gen. 338 (2008) 100–113, https://doi.org/10.1016/j.apcata.2007.12.026.
[30] X. Li, R. Prins, J.A. van Bokhoven, Synthesis and characterization of mesoporous mordenite, J. Catal. 262 (2009) 257–265, https://doi.org/10.1016/j.jcat.2009.01.001.
[31] U. Olsbye, S. Svelle, M. Bjørgen, P. Beato, T.V.W. Janssens, F. Joensen, et al., Conversion of methanol to hydrocarbons: how zeolite cavity and pore size controls product selectivity, Angew. Chem. Int. Ed. 51 (2012) 5810–5831, https://doi.org/10.1002/anie.201103657.
[32] S. Soltanian, C.L. Lee, S.S. Lam, A review on the role of hierarchical zeolites in the production of transportation fuels through catalytic fast pyrolysis of biomass, Biofuel Res J 7 (2020) 1217–1234, https://doi.org/10.18331/BRJ2020.7.3.5.
[33] T.K. Dada, M.A. Islam, A.K. Vuppaladadiyam, E. Antunes, Thermo-catalytic co-pyrolysis of ironbark sawdust and plastic waste over strontium loaded hierarchical Y-zeolite, J. Environ. Manag. 299 (2021), 113610, https://doi.org/10.1016/j.jenvman.2021.113610.
[34] R. Sato, Z. Liu, C. Peng, C. Tan, P. Hu, J. Zhu, et al., Engineering mesopore formation in hierarchical zeolites under high hydrostatic pressure, Chem. Mater. 33 (2021) 8440–8446, https://doi.org/10.1021/acs.chemmater.1c02800.
[35] K.A. Tarach, K. Góra-Marek, J. Martinez-Triguero, I. Melián-Cabrera, Acidity and accessibility studies of desilicated ZSM-5 zeolites in terms of their effectiveness as catalysts in acid-catalyzed cracking processes, Catal. Sci. Technol. 7 (2017) 858–873, https://doi.org/10.1039/C6CY02609E.
[36] J. Pérez-Ramírez, D. Verboekend, A. Bonilla, S. Abelló, Zeolite catalysts with tunable hierarchy factor by pore-growth moderators, Adv. Funct. Mater. 19 (2009) 3972–3979, https://doi.org/10.1002/adfm.200901394.
[37] S. Sartipi, K. Parashar, M.J. Valero-Romero, V.P. Santos, B. van der Linden, M. Makkee, et al., Hierarchical H-ZSM-5-supported cobalt for the direct synthesis of gasoline-range hydrocarbons from syngas: advantages, limitations, and mechanistic insight, J. Catal. 305 (2013) 179–190, https://doi.org/10.1016/j.jcat.2013.05.012.
[38] C.S. Costa, M. Muñoz, M.R. Ribeiro, J.M. Silva, H-USY and H-ZSM-5 zeolites as catalysts for HDPE conversion under a hydrogen reductive atmosphere, Sustain. Energy Fuels 5 (2021) 1134–1147, https://doi.org/10.1039/D0SE01584A.
[39] F. Gorzin, J. Towfighi Darian, F. Yaripour, S.M. Mousavi, Preparation of hierarchical HZSM-5 zeolites with combined desilication with NaAlO 2/ tetrapropylammonium hydroxide and acid modification for converting methanol to propylene, RSC Adv. 8 (2018) 41131–41142, https://doi.org/10.1039/C8RA08624A.
[40] O. Daoura, M.-N. Kaydouh, N. El-Hassan, P. Massiani, F. Launay, M. Boutros, Mesocellular silica foam-based Ni catalysts for dry reforming of CH4 (by CO2), J. CO2 Util. 24 (2018) 112–119, https://doi.org/10.1016/j.jcou.2017.12.010.
[41] M. Al-Naji, A.M. Balu, A. Roibu, M. Goepel, W.-D. Einicke, R. Luque, et al., Mechanochemical preparation of advanced catalytically active bifunctional Pd-containing nanomaterials for aqueous phase hydrogenation, Catal. Sci. Technol. 5 (2015) 2085–2091, https://doi.org/10.1039/C4CY01174K.
[42] S. Habib, F. Launay, M.-A. Springuel-Huet, F. Guenneau, M. Mazaj, N. Novak Tušar, et al., Hyperpolarized 129Xe NMR and N2 sorption cross-investigations of the crystallization of Al-SBA-15 amorphous walls into ZSM-5 type materials, J. Porous Mater. 16 (2009) 349–359, https://doi.org/10.1007/s10934-008-9207-x.
[43] V.A. Nguyen, M. Ramanathan, Application of Brunauer–Emmett–Teller (BET) theory and the Guggenheim–Anderson–de Boer (GAB) equation for concentration-dependent, non-saturable cell–cell interaction dose-responses, J. Pharmacokinet. Pharmacodyn. 47 (2020) 561–572, https://doi.org/10.1007/s10928-020-09708-x.
[44] G. Leofanti, M. Padovan, G. Tozzola, B. Venturelli, Surface area and pore texture of catalysts, Catal. Today 41 (1998) 207–219, https://doi.org/10.1016/S0920-5861(98)00050-9.
[45] V. Zholobenko, C. Freitas, M. Jendrlin, P. Bazin, A. Travert, F. Thibault-Starzyk, Probing the acid sites of zeolites with pyridine: quantitative AGIR measurements of the molar absorption coefficients, J. Catal. 385 (2020) 52–60, https://doi.org/10.1016/j.jcat.2020.03.003.
[46] G.C. Bond, Small Metal Particles and Supported Metal Catalysts. Met. React. Hydrocarb., Springer US, 2005, pp. 35–91, https://doi.org/10.1007/0-387-26111-7_2.
[47] C.S. Costa, H. Dao Thi, K.M. Van Geem, M. Rosário Ribeiro, J.M. Silva, Assessment of acidity and the zeolite porous structure on hydrocracking of HDPE, Sustain. Energy Fuels 6 (2022) 3611–3625, https://doi.org/10.1039/D2SE00497F.
[48] S. Yang, C. Yu, L. Yu, S. Miao, M. Zou, C. Jin, et al., Bridging dealumination and desilication for the synthesis of hierarchical MFI zeolites, Angew. Chem. 129 (2017) 12727–12730, https://doi.org/10.1002/ange.201706566.
[49] D. Verboekend, J.C. Groen, J. Pérez-Ramírez, Interplay of properties and functions upon introduction of mesoporosity in ITQ-4 zeolite, Adv. Funct. Mater. 20 (2010) 1441–1450, https://doi.org/10.1002/adfm.200902205.
[50] D. Verboekend, J. Pérez-Ramírez, Design of hierarchical zeolite catalysts by desilication, Catal. Sci. Technol. 1 (2011) 879, https://doi.org/10.1039/c1cy00150g.
[51] D. Verboekend, S. Mitchell, M. Milina, J.C. Groen, J. Pérez-Ramírez, Full compositional flexibility in the preparation of mesoporous MFI zeolites by desilication, J. Phys. Chem. C 115 (2011) 14193–14203, https://doi.org/10.1021/jp201671s.
[52] W. Wang, F. Xin, Y. Tu, Z. Wang, Pore structure development in Xilingol lignite under microwave irradiation, J. Energy Inst. 91 (2018) 75–86, https://doi.org/10.1016/j.joei.2016.10.005.
[53] S. Wu, Y. Wang, C. Sun, T. Zhao, J. Zhao, Z. Wang, et al., Novel preparation of binder-free Y/ZSM-5 zeolite composites for VOCs adsorption, Chem. Eng. J. 417 (2021), 129172, https://doi.org/10.1016/j.cej.2021.129172.
[54] O. Daoura, M. Boutros, O. Daoura, F. Launay, P. Massiani, N. EL Hassan, Influence of synthesis parameters of mesocellular silica foams doped by nickel on methane reforming by CO 2, MATEC Web Conf 171 (2018), 03002, https://doi.org/10.1051/matecconf/201817103002.
[55] S. Habib, F. Launay, H El Zakhem, M. Mazaj, F. Guenneau, P. Beaunier, et al., ZSM-5/SBA-15 microporous/mesoporous composites prepared by a microwave-assisted zeolitisation of Al-SBA-15 mesoporous solids, Mater. Res. Bull. 48 (2013) 1288–1295, https://doi.org/10.1016/j.materresbull.2012.12.030.
[56] W.C. Conner, G. Tompsett, K.-H. Lee, K.S. Yngvesson, Microwave synthesis of zeolites: 1. Reactor engineering, J. Phys. Chem. B 108 (2004) 13913–13920, https://doi.org/10.1021/jp037358c.
[57] M. Milina, S. Mitchell, P. Crivelli, D. Cooke, J. Pérez-Ramírez, Mesopore quality determines the lifetime of hierarchically structured zeolite catalysts, Nat. Commun. 5 (2014) 3922, https://doi.org/10.1038/ncomms4922.
[58] S.R. Batool, V.L. Sushkevich, J.A. van Bokhoven, Correlating Lewis acid activity to extra-framework aluminum species in zeolite Y introduced by Ion-exchange, J. Catal. 408 (2022) 24–35, https://doi.org/10.1016/j.jcat.2022.02.010.
[59] N. Brodu, M.-H. Manero, C. Andriantsiferana, J.-S. Pic, H. Valdés, Role of Lewis acid sites of ZSM-5 zeolite on gaseous ozone abatement, Chem. Eng. J. 231 (2013) 281–286, https://doi.org/10.1016/j.cej.2013.07.002.
[60] M.S. Holm, S. Svelle, F. Joensen, P. Beato, C.H. Christensen, S. Bordiga, et al., Assessing the acid properties of desilicated ZSM-5 by FTIR using CO and 2,4,6-trimethylpyridine (collidine) as molecular probes, Appl. Catal. Gen. 356 (2009) 23–30, https://doi.org/10.1016/j.apcata.2008.11.033.
[61] M. Milina, S. Mitchell, N.-L. Michels, J. Kenvin, J. Pérez-Ramírez, Interdependence between porosity, acidity, and catalytic performance in hierarchical ZSM-5 zeolites prepared by post-synthetic modification, J. Catal. 308 (2013) 398–407, https://doi.org/10.1016/j.jcat.2013.08.020.

[62] R.T.J. Gerards, A. Fernandes, I. Graça, M.F. Ribeiro, Towards understanding of phenolic compounds impact on Ni- and V-USY zeolites during bio-oils co-processing in FCC units, Fuel 260 (2020), 116372, https://doi.org/10.1016/j.fuel.2019.116372.
[63] Z. Wang, K.-D. Kim, C. Zhou, M. Chen, N. Maeda, Z. Liu, et al., Influence of support acidity on the performance of size-confined Pt nanoparticles in the chemoselective hydrogenation of acetophenone, Catal. Sci. Technol. 5 (2015) 2788–2797, https://doi.org/10.1039/C5CY00214A.
[64] M. Boronat, A. Corma, What is measured when measuring acidity in zeolites with probe molecules? ACS Catal. 9 (2019) 1539–1548, https://doi.org/10.1021/acscatal.8b04317.
[65] D.J. Parrillo, A.T. Adamo, G.T. Kokotailo, R.J. Gorte, Amine adsorption in H-ZSM-5, Appl. Catal. 67 (1990) 107–118, https://doi.org/10.1016/S0166-9834(00)84435-8.
[66] J. Socci, A. Saraeian, S.D. Stefanidis, S.W. Banks, B.H. Shanks, T. Bridgwater, The role of catalyst acidity and shape selectivity on products from the catalytic fast pyrolysis of beech wood, J. Anal. Appl. Pyrolysis 162 (2022), 104710, https://doi.org/10.1016/j.jaap.2019.104710.
[67] X. Xian, M. He, Y. Gao, Y. Bi, Y. Chu, J. Chen, et al., Acidity tuning of HZSM-5 zeolite by neutralization titration for coke inhibition in supercritical catalytic cracking of n-dodecane, Appl. Catal. Gen. 623 (2021), 118278, https://doi.org/10.1016/j.apcata.2021.118278.
[68] R.G. Leliveld B, J.H.V. Kerkhoffs M, A. Broersma F, A.J. van Dillen J, W. Geus J, C. Koningsberger D, Acidic properties of synthetic saponites studied by pyridine IR and TPD[ndash]TG of n-propylamine, J. Chem. Soc. Faraday. Trans. 94 (1998) 315, https://doi.org/10.1039/a705357f.
[69] A. Zecchina, S. Bordiga, G. Spoto, D. Scarano, G. Petrini, G. Leofanti, et al., Low-temperature Fourier-transform infrared investigation of the interaction of CO with nanosized ZSM5 and silicalite, J. Chem. Soc., Faraday Trans. 88 (1992) 2959–2969, https://doi.org/10.1039/FT9928802959.
[70] K. Sadowska, K. Góra-Marek, J. Datka, Accessibility of acid sites in hierarchical zeolites: quantitative IR studies of pivalonitrile adsorption, J. Phys. Chem. C 117 (2013) 9237–9244, https://doi.org/10.1021/jp400400t.
[71] B. Puértolas, A. Veses, M.S. Callén, S. Mitchell, T. García, J. Pérez-Ramírez, Porosity-acidity interplay in hierarchical ZSM-5 zeolites for pyrolysis oil valorization to aromatics, ChemSusChem 8 (2015) 3283–3293, https://doi.org/10.1002/cssc.201500685.
[72] S. Li, A. Zheng, Y. Su, H. Zhang, L. Chen, J. Yang, et al., Brønsted/lewis acid synergy in dealuminated HY zeolite: a combined solid-state nmr and theoretical calculation study, J. Am. Chem. Soc. 129 (2007) 11161–11171, https://doi.org/10.1021/ja072767y.
[73] C.J.A. Mota, D.L. Bhering, N. Rosenbach, A DFT study of the acidity of ultrastable Y zeolite: where is the brønsted/lewis acid synergism? Angew. Chem. Int. Ed. 43 (2004) 3050–3053, https://doi.org/10.1002/anie.200353049.
[74] G. Crépeau, V. Montouillout, A. Vimont, L. Mariey, T. Cseri, F. Maugé, Nature, structure and strength of the acidic sites of amorphous silica alumina: an IR and NMR study, J. Phys. Chem. B 110 (2006) 15172–15185, https://doi.org/10.1021/jp062252d.
[75] E. Brunner, Magic-angle-spinning NMR studies of acid sites in zeolite H-ZSM-5, J. Catal. 127 (1991) 34–41, https://doi.org/10.1016/0021-9517(91)90206-J.
[76] N. Pannilawithana, C.S. Yi, Catalytic carbon–carbon bond activation of saturated and unsaturated carbonyl compounds via chelate-assisted coupling reaction with indoles, ACS Catal. 10 (2020) 5852–5861, https://doi.org/10.1021/acscatal.0c01245.
[77] J. Abbot, Role of Brønsted and Lewis acid sites during cracking reactions of alkanes, Appl. Catal. 47 (1989) 33–44, https://doi.org/10.1016/S0166-9834(00)83260-1.
[78] S. Müller, Y. Liu, F.M. Kirchberger, M. Tonigold, M. Sanchez-Sanchez, J.A. Lercher, Hydrogen transfer pathways during zeolite catalyzed methanol conversion to hydrocarbons, J. Am. Chem. Soc. 138 (2016) 15994–16003, https://doi.org/10.1021/jacs.6b09605.
[79] I. Istadi, T. Riyanto, L. Buchori, D.D. Anggoro, G. Gilbert, K.A. Meiranti, et al., Enhancing brønsted and Lewis acid sites of the utilized spent RFCC catalyst waste for the continuous cracking process of palm oil to biofuels, Ind. Eng. Chem. Res. 59 (2020) 9459–9468, https://doi.org/10.1021/acs.iecr.0c01061.
[80] K. Li, S. Lee, G. Yuan, J. Lei, S. Lin, P. Weerachanchai, et al., Investigation into the catalytic activity of microporous and mesoporous catalysts in the pyrolysis of waste polyethylene and polypropylene mixture, Energies 9 (2016) 431, https://doi.org/10.3390/en9060431.
[81] A. Coelho, L. Costa, M.M. Marques, I.M. Fonseca, M.A.N.D.A. Lemos, F. Lemos, The effect of ZSM-5 zeolite acidity on the catalytic degradation of high-density polyethylene using simultaneous DSC/TG analysis, Appl. Catal. Gen. 413–414 (2012) 183–191, https://doi.org/10.1016/j.apcata.2011.11.010.
[82] W. Ding, J. Liang, L.L. Anderson, Thermal and catalytic degradation of high density polyethylene and commingled post-consumer plastic waste, Fuel Process. Technol. 51 (1997) 47–62, https://doi.org/10.1016/S0378-3820(96)01080-6.
[83] G. Manos, A. Garforth, J. Dwyer, Catalytic degradation of high-density polyethylene over different zeolitic structures, Ind. Eng. Chem. Res. 39 (2000) 1198–1202, https://doi.org/10.1021/ie990512q.
[84] J.W. Park, J.-H. Kim, G. Seo, The effect of pore shape on the catalytic performance of zeolites in the liquid-phase degradation of HDPE, Polym. Degrad. Stabil. 76 (2002) 495–501, https://doi.org/10.1016/S0141-3910(02)00059-9.